

The SAURON project – XVII. Stellar population analysis of the absorption line strength maps of 48 early-type galaxies

Harald Kuntschner,^{1*} Eric Emsellem,^{2,3} Roland Bacon,³ Michele Cappellari,⁴ Roger L. Davies,⁴ P. Tim de Zeeuw,^{2,5} Jesús Falcón-Barroso,⁶ Davor Krajnović,² Richard M. McDermid,⁷ Reynier F. Peletier,⁸ Marc Sarzi,⁹ Kristen L. Shapiro,¹⁰ Remco C. E. van den Bosch¹¹ and Glenn van de Ven¹²

¹Space Telescope European Coordinating Facility, European Southern Observatory, Karl-Schwarzschild-Str. 2, 85748 Garching, Germany

²European Southern Observatory, Karl-Schwarzschild-Str 2, 85748 Garching, Germany

³Centre de Recherche Astronomique de Lyon, 9 Avenue Charles André, 69230 Saint Genis Laval, France

⁴Sub-department of Astrophysics, University of Oxford, Denys Wilkinson Building, Keble Road, Oxford OX1 3RH

⁵Sterrewacht Leiden, Universiteit Leiden, Postbus 9513, 2300 RA Leiden, the Netherlands

⁶Instituto de Astrofísica de Canarias, Canarias, Via Lactea s/n, 38700 La Laguna, Tenerife, Spain

⁷Gemini Observatory, Northern Operations Center, 670 N. Aohoku Place, Hilo, HI 96720, USA

⁸Kapteyn Astronomical Institute, Rijksuniversiteit Groningen, Postbus 800, 9700 AV Groningen, the Netherlands

⁹Centre for Astrophysics Research, University of Hertfordshire, College Lane, Hatfield, Herts AL10 9AB

¹⁰UC Berkeley Department of Astronomy, Berkeley, CA 94720, USA

¹¹Department of Astronomy, University of Texas, Austin, TX 78712, USA

¹²Max Planck Institute for Astronomy, D-69117 Heidelberg, Germany

Accepted 2010 June 2. Received 2010 June 2; in original form 2010 February 22

ABSTRACT

We present a stellar population analysis of the absorption line strength maps for 48 early-type galaxies from the SAURON sample. Using the line strength index maps of $H\beta$, Fe5015 and Mg b , measured in the Lick/IDS system and spatially binned to a constant signal-to-noise ratio, together with predictions from up-to-date stellar population models, we estimate the simple stellar population-equivalent (SSP-equivalent) age, metallicity and abundance ratio $[\alpha/\text{Fe}]$ over a two-dimensional field extending up to approximately one effective radius. A discussion of calibrations and differences between model predictions is given. Maps of SSP-equivalent age, metallicity and abundance ratio $[\alpha/\text{Fe}]$ are presented for each galaxy. We find a large range of SSP-equivalent ages in our sample, of which ~ 40 per cent of the galaxies show signs of a contribution from a young stellar population. The most extreme cases of post-starburst galaxies, with SSP-equivalent ages of ≤ 3 Gyr observed over the full field-of-view, and sometimes even showing signs of residual star formation, are restricted to low-mass systems ($\sigma_e \leq 100 \text{ km s}^{-1}$ or $\sim 2 \times 10^{10} M_\odot$). Spatially restricted cases of young stellar populations in circumnuclear regions can almost exclusively be linked to the presence of star formation in a thin, dusty disc/ring, also seen in the near-UV or mid-IR on top of an older underlying stellar population.

The flattened components with disc-like kinematics previously identified in all fast rotators are shown to be connected to regions of distinct stellar populations. These range from the young, still star-forming circumnuclear discs and rings with increased metallicity preferentially found in intermediate-mass fast rotators, to apparently old structures with extended disc-like kinematics, which are observed to have an increased metallicity and mildly depressed $[\alpha/\text{Fe}]$ ratio compared to the main body of the galaxy. The slow rotators, often harbouring kinematically decoupled components (KDC) in their central regions, generally show no

*E-mail: hkuntsch@eso.org

stellar population signatures over and above the well-known metallicity gradients in early-type galaxies and are largely consistent with old (≥ 10 Gyr) stellar populations.

Using radially averaged stellar population gradients we find in agreement with Spolaor et al. a mass–metallicity gradient relation where low-mass fast rotators form a sequence of increasing metallicity gradient with increasing mass. For more massive systems (above $\sim 3.5 \times 10^{10} M_{\odot}$) there is an overall downturn such that metallicity gradients become shallower with increased scatter at a given mass leading to the most massive systems being slow rotators with relatively shallow metallicity gradients. The observed shallower metallicity gradients and increased scatter could be a consequence of the competition between different star formation and assembly scenarios following a general trend of diminishing gas fractions and more equal-mass mergers with increasing mass, leading to the most massive systems being devoid of ordered motion and signs of recent star formation.

Key words: galaxies: bulges – galaxies: elliptical and lenticular, cD – galaxies: evolution – galaxies: formation – galaxies: kinematics and dynamics – galaxies: nuclei.

1 INTRODUCTION

In hierarchical galaxy formation models with a Λ -dominated cold dark matter (Λ CDM) cosmology, early-type galaxies are predicted to have formed through the merging of smaller galaxies and accretion events over time (e.g. Somerville & Primack 1999; Cole et al. 2000; Bower et al. 2006; De Lucia et al. 2006). Large galaxy surveys in the local Universe as well as at medium redshift have shown that galaxies follow a strong bimodality in colour–magnitude space, forming a ‘red sequence’ and a ‘blue cloud’ with an intermediate region sparsely populated by galaxies sometimes dubbed the ‘green valley’ (e.g. Baldry et al. 2004; Bell et al. 2004; Willmer et al. 2006). The hierarchical galaxy formation scenario has received renewed observational support by the recent findings of the COMBO-17 and DEEP2 surveys that the stellar mass of galaxies on the red sequence has increased by a factor of 2–5 since redshift $z \sim 1$ (Bell et al. 2004; Faber et al. 2007; but see Marchesini et al. 2009). This growth of mass can arise from two main sources: (1) the growth of objects already on the red sequence (in the case of cold gas accretion they may move from the red sequence into the ‘green valley’ during the period of star formation) and (2) the addition of galaxies from the blue cloud once star formation is shut off either by consumption or by the removal of the cold gas reservoir (Faber et al. 2007).

There is observational evidence that the detailed growth of mass on the red sequence is a function of luminosity (here used as a proxy for total galaxy mass) as well as a function of environment. While most massive galaxies have already joined the red sequence at $z \sim 1$ (Treu et al. 2005; Bundy et al. 2006; Cimatti, Daddi & Renzini 2006), the low-mass end of the red sequence seems to be subject to the continued arrival and re-rejuvenation of galaxies up to the present day [Treu et al. 2005; Schawinski et al. 2007; Sansom & Northeast 2008; Smith et al. 2009; Shapiro et al. 2010 (hereafter Paper XV) but see Trager, Faber & Dressler 2008]. Taken together, a scenario emerges where low-mass early-type galaxies (on the red sequence), irrespective of their environment, are predicted to show younger stellar population ages than their more massive counterparts. In addition, galaxies residing in high-density environments are older and show less spread in stellar age than those in less dense regions (see also Trager et al. 2008).

Many authors have investigated the scenarios summarized above by means of a stellar population analysis of nearby early-type galax-

ies based on optical line strength indices often measured in the Lick/IDS system. In most of the studies galaxies are treated as spatially unresolved sources (e.g. Bernardi et al. 2006; Yamada et al. 2006; Schawinski et al. 2007; Trager et al. 2008; Thomas et al. 2010) allowing access to either large samples of galaxies, as for example in the case of the Sloan Digital Sky Survey (York et al. 2000), or the analysis of extremely high signal-to-noise ratio (S/N) data. Only a limited number of studies have investigated line strength gradients obtained with long slits (e.g. Davies, Sadler & Peletier 1993; Sánchez-Blázquez et al. 2007; Spolaor et al. 2009) or radially averaging the data from integral-field-units (Rawle et al. 2008); spatially resolved stellar population maps of early-type galaxies remain the exception (e.g. McDermid et al. 2006, Paper VIII; Blanc et al. 2009; Chilingarian 2009; Pracy et al. 2009).

With the advent of high throughput integral field units on medium-sized telescopes, the study of two-dimensional stellar populations maps has become feasible. We have conducted a survey of 72 representative early-type (E, S0, and Sa) galaxies using the integral-field spectrograph SAURON mounted on the William Herschel Telescope in La Palma (Bacon et al. 2001; de Zeeuw et al. 2002). This allowed us to map the stellar and gas kinematics as well as a number of stellar absorption line indices up to about one effective radius R_e for most of the galaxies in the sample. Analysing the global properties of the velocity fields of the 48 E and S0 galaxies Emsellem et al. (2007, hereafter Paper IX) characterized the population of early-type galaxy with two classes of slow and fast rotators, according to their specific (projected) angular momentum measured within one effective radius, λ_R . Krajnović et al. (2008, hereafter Paper XII) further analysed the velocity and velocity dispersion maps using kinometry, a generalization of surface photometry to the higher order moments of the line-of-sight velocity distribution (Krajnović et al. 2006) and found that 74 per cent of Es and 92 per cent of S0s in the SAURON sample exhibit rotation, which can be well described by that of a simple, inclined disc. Scott et al. (2009) explore the surprisingly tight correlation between the local escape velocity V_{esc} and stellar population parameters.

In this paper, we present for the 48 E and S0 galaxies in the SAURON sample estimates of the mean simple stellar population-equivalent (hereafter SSP-equivalent; see Trager et al. 2008) stellar population parameters, age, metallicity and abundance ratio $[\alpha/\text{Fe}]$ for each bin in our maps. The study is based on the line strength

measurements presented in Kuntschner et al. (2006, hereafter Paper VI), although we provide a short description of an improved data-reduction scheme and the resulting updated line strength measurements in this paper. Compared to many other line strength based stellar population studies, our work rests on a limited number (three to four) of line strength indices. However, our study has the benefit of covering a contiguous region of the galaxies, often reaching out to approximately one effective radius R_e . Furthermore, it complements and extends the SAURON survey studies of the *Galaxy Evolution Explorer* satellite (hereafter *GALEX*) near-UV (hereafter NUV) imaging (Jeong et al. 2009, hereafter Paper XIII), *Spitzer Space Telescope* mid-IR imaging (Paper XV) and ionized gas (Sarzi et al. 2010, hereafter Paper XVI).

This paper is organized as follows. In Section 2, we present the details of our revised data reduction leading to improved line strength measurements. In Section 3, we describe our method to estimate stellar population parameters from the available set of Lick/IDS indices along with a discussion on the reliability of the results. The two-dimensional stellar population maps are presented in Section 4, where we first discuss in detail the findings and also analyse overall stellar population gradients and scaling relations of the aperture measurements with central velocity dispersion and dynamical mass of the galaxies. The conclusions follow in Section 5. We present a revised table of circular aperture line strength measurements within $R_e/8$ and one R_e in the Appendix.

2 REVISED DATA REDUCTION

The results presented here are based on the observations and data reduction described in Emsellem et al. (2004, hereafter Paper III), Paper VI and Sarzi et al. (2006, hereafter Paper V). However, our spectral template library which is used to derive the kinematics and the gas emission was changed from the Jones library (Jones 1999) to the stars from the recently published Medium resolution INT Library of Empirical Spectra (hereafter MILES; Sánchez-Blázquez et al. 2006). This new library provides better fits to our spectra, therefore minimizing template mismatch (see also Cappellari et al. 2007). The main consequences of this are small, but significant changes to the kinematics; namely reduced σ and h_4 values where the change is most significant in the central regions of our sample galaxies and over a larger area for the most massive systems. These changes in the kinematics carry through to the fully corrected line strength measurements via the internal velocity broadening corrections and result in slightly reduced values for Mg *b*, Fe5015 and Fe5270_S in the affected regions of the maps (see Paper VI).

In an attempt to further improve the emission-line corrections to our absorption line strength measurements, we also re-extracted the nebular emission fluxes and kinematics using the MILES stellar library. In the case of emission-line measurements, however, it is crucial to provide an underlying fit to the stellar continuum that is as physically motivated as possible in order to avoid spurious results. For this reason, rather than using a subset of stellar spectra from the MILES library for each separate galaxy, we used for the entire sample a single-template library consisting of 48 SSP models from Vazdekis et al. (2010, based on MILES stellar spectra) to which we added a number of stellar templates obtained by matching SAURON spectra devoid of emission. Specifically, based on the maps of Paper V, we extracted 50 high S/N spectra from circular apertures in regions without significant emission. We fitted these with the MILES stars over the *entire* wavelength range (i.e. without excluding regions prone to emission), excluding only the stellar templates with exceedingly low ($<0.9 \text{ \AA}$) values of the H β absorption-line

strength. The optimal combination of the stellar spectra that best matched each of our emission-free aperture spectra constitute each of the empirical templates in our new template library. Care was taken to extract SAURON spectra covering the range of absorption-line strengths observed in Paper VI. Therefore, our empirical templates approximate as closely as possible the spectra of real early-type galaxies, were they unaffected by kinematic broadening.

Although adopting the new template library does not lead to a dramatically better sensitivity in the detection of nebular emission, the use of such a physically motivated set of templates leads to more robust emission-line measurements, and therefore a better correction of the absorption-line strength indices affected by emission (mostly H β and Fe5015 in our survey). For further discussion of the new emission-line measurements see Paper XVI.

In summary, the use of the new spectral template library significantly improved the measurements of the line strength indices. Main results presented in earlier papers, however, are not affected. Specifically, in Paper VI we presented a comparison between the isoindex contours of Mg *b* and the isophotes of the surface brightness finding that the Mg *b* contours appear to be flatter for about 40 per cent of our galaxies without significant dust features. Using the revised index measurements, we find that ellipticity measurements for the Mg *b* contours have slightly changed, but agree within the one σ errors with the previous measurements. Furthermore, the stellar M/L ratios derived in Cappellari et al. (2006) remain the same within the quoted errors.

In Table A1, we present the updated line strength measurements for circular apertures within $R_e/8$ and one R_e . These values supersede the ones presented in Paper VI. Aperture line strength measurements changed by less than 17 per cent with robustly measured mean offsets of 0.12, -0.37 , -0.02 and 0.00 \AA for the H β , Fe5015, Mg *b* and Fe5270_S indices over the ($R_e/8$) aperture, respectively. For the one R_e aperture, the offsets are 0.12, -0.31 , -0.01 for the H β , Fe5015 and Mg *b* indices, respectively. Note that we also made use of the revised estimates of the effective radii R_e (see Table A1) which were derived with a $R^{1/n}$ growth curve analysis from our wide-field MDM (1.3 m) imaging survey of the SAURON sample (Falcón-Barroso, in preparation).

3 ESTIMATING STELLAR POPULATION PARAMETERS

Estimates of luminosity-weighted stellar population parameters such as age, metallicity and abundance ratios can be inferred from a set of line strength indices measured on integrated spectra in combination with the predictions from stellar population models. In this section, we begin by presenting a first-order overview of the ages and metallicities of our sample galaxies using classical age/metallicity diagnostic diagrams and then describe the χ^2 technique used for the full analysis of our data including the abundance ratio variations.

3.1 A first look with classical techniques

The classical problem of the degeneracy between age and metallicity changes in an old (≥ 2 Gyr) integrated stellar population can be partially overcome by plotting a combination of metallicity-sensitive indices against an age-sensitive index (e.g. Worthey 1994). This method has been used successfully in the past, and we will present an overview of our data with this traditional method before we employ state-of-the-art techniques for the full analysis of our line strength maps (see Section 3.2).

Due to our limited wavelength range (4800–5380 Å) we can only use $H\beta$ as an age-sensitive index. In order to minimize the influence of abundance ratio variations on our first-order age estimates derived from the classical index *versus* index diagrams we define composite indices. These indices are constructed such that a mean metallicity is measured rather than a metallicity biased to one species. The $H\beta$ index shows only a mild dependence on abundance ratios (e.g. Thomas, Maraston & Bender 2003, hereafter TMB03) and can be safely used in a first-order analysis. We emphasize that these composite indices are largely used for presentation purposes when we want to show our measurements in the observational plane of index *versus* index diagrams.

Within the SAURON wavelength range, we measure three different metallicity indicators: Fe5015, $Mg\ b$ and Fe5270_s (for details see Paper VI). These indices are not pure metallicity indicators, but are also sensitive to age changes. Furthermore, non-solar abundance ratios can severely affect the interpretation of these indices if not taken into account (e.g. Kuntschner et al. 2001, TMB03). In practice, it is sometimes convenient to define metallicity indicators which are insensitive to abundance ratio variations. The first index¹ of this sort was defined by González (1993) and further improved by TMB03.² However, the SAURON wavelength range does not allow us to measure Fe5335. Therefore, we define new, abundance-ratio-insensitive index combinations for the available indices. We follow the approach by TMB03 and also use their models to derive the index definitions. The subset of the model library we use to define the new indices spans ages from 1 to 15 Gyr, metallicities from $[Z/H] = -1.35$ to 0.35, and abundance ratios of $[\alpha/Fe] = 0.0$ to 0.5. This covers most of the range of stellar population parameters which we probe in this survey.

The new abundance ratio insensitive indices are defined as

$$[MgFe52]' = \frac{0.64 \times Mg\ b + Fe5270}{2} \quad (1)$$

$$[MgFe50]' = \frac{0.69 \times Mg\ b + Fe5015}{2}. \quad (2)$$

The scaling factor for the $Mg\ b$ index was optimized so that the mean difference between solar and non-solar models is zero for this index. Fig. 1 demonstrates that, similar to the $[MgFe]'$ index defined by TMB03, the new composite indices are rather insensitive to abundance ratio changes over the range probed by the model predictions.

In Fig. 2, we show the relation between $[MgFe52]'$ and $[MgFe50]'$ *versus* $[MgFe]'$ for a sample of well-calibrated Fornax early-type galaxies taken from Kuntschner (2000). There is a good linear correlation between the new composite indices and $[MgFe]'$ as expected if they are good indicators of mean metallicity.

Throughout this paper, we use index measurements calibrated to the Lick/IDS system (see Paper VI and Section 2). There are various stellar population models available for this system (e.g. TMB03; Worthey 1994; Vazdekis et al. 1997; Lee & Worthey 2005; Schiavon 2007) which agree to the first order in their predictions of index strength as the function of age, metallicity and abundance ratio, but differ in details. We demonstrate this in Fig. 3 where we show radial gradients averaged along lines of constant surface brightness in the $H\beta$ *versus* $[MgFe50]'$ plane for the 48 early-type galaxies in our sample. The centre of each galaxy is indicated by

¹ $[MgFe] = \sqrt{Mg\ b \times \frac{(Fe5270 + Fe5335)}{2}}$.

² $[MgFe]' = \sqrt{Mg\ b \times (0.72 \times Fe5270 + 0.28 \times Fe5335)}$.

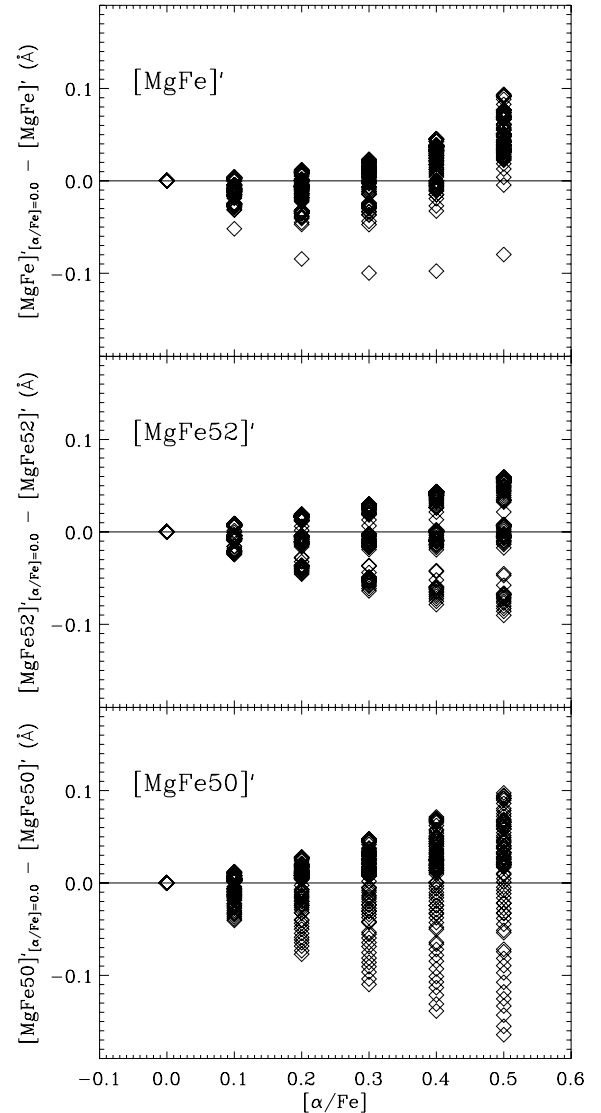


Figure 1. The dependence of $[MgFe]'$ (TMB03), $[MgFe52]'$ and $[MgFe50]'$ on abundance ratio $[\alpha/Fe]$. Shown is the difference between the model predictions (TMB03) at solar abundance ratio and the model predictions for non-solar abundance ratios. The model library used here spans ages from 1 to 15 Gyr, metallicities from $[Z/H] = -1.35$ to 0.35 and abundance ratios of $[\alpha/Fe] = 0.0$ to 0.5.

a filled circle. Overplotted are model predictions from Schiavon (2007)³ for $[\alpha/Fe] = 0.0$ on the left and model predictions by TMB03 for $[\alpha/Fe] = 0.0$ on the right. This diagram provides a convenient overview of our line strength measurements while at the same time graphically showing the relation between the stellar population parameters, luminosity-weighted age and metallicity, as predicted by the models.

It is evident from the plot and consistent for both stellar population models that the galaxies span a large range in luminosity-weighted age with the majority of galaxies clustering at old ages (~ 12 Gyr). However, taking an ~ 9 Gyr isochrone as a dividing line,

³ We use here the ‘base’ models from Schiavon (2007) with solar abundance ratios, where the abundance ratio bias of the stellar library has been removed. The model predictions were transformed to the Lick system by using the offsets described in table 1 of Schiavon (2007).

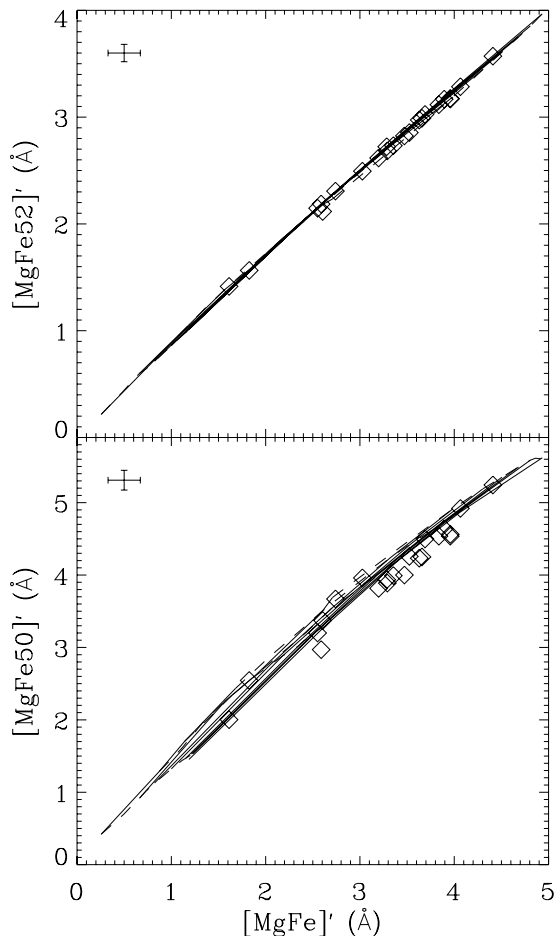


Figure 2. $[\text{MgFe}52]'$ and $[\text{MgFe}50]'$ versus $[\text{MgFe}]'$ for a sample of Fornax galaxies taken from Kuntschner (2000) are shown as open diamonds. Overplotted are stellar population models by TMB03 at solar abundance ratio. Average error bars for the Fornax data are shown in the upper-left corner. Note, however, that the errors are correlated due to some indices being used in both axes.

about 40 per cent of our sample galaxies show signs for the presence of young stellar populations. Excluding the very youngest objects, radial line strength gradients translate into a decline in metallicity with increasing radius.

Examining the diagram in more detail, one can see that most galaxies that are dominated by old stellar populations (e.g. age >9 Gyr) exhibit roughly constant $H\beta$ absorption strength with radius (see also Paper VI). Taken at face value, the TMB03 models predict for those galaxies an age gradient such that the centre is younger than the outskirts. Moreover, a significant fraction of galaxies shows $H\beta$ strengths at large radii which are below the model predictions for an age of 15 Gyr. Using the Schiavon (2007) models, both effects are mitigated in the sense that there is little or no evidence for age gradients for old galaxies and that the majority of line strength measurements lie within the range of model predictions.

The TMB03 and Schiavon models both use the same index sensitivity functions from Korn, Maraston & Thomas (2005) to correct for abundance ratio patterns, however they use different stellar libraries, namely the Jones (1999) library in the Schiavon models and the Lick/IDS library (Worthey et al. 1994) in TMB03.

Although the Schiavon (2007) models appear to better fit the observational data of the SAURON survey, we emphasize that stellar population models are not considered perfect by us and calibration

uncertainties between the models and observed data remain an issue (see also Graves & Schiavon 2008). For the remainder of this paper we will use the models of Schiavon (2007) for our stellar population analysis. However, we will make specific reference to TMB03 at key points to demonstrate the model independence of our results.

3.2 The χ^2 technique

In the classical index–index diagrams described above, one typically does not make use of all available index measurements, and furthermore it requires an iterative scheme if one is interested in abundance ratio estimates. A more elegant way of determining stellar population parameters is the χ^2 technique (e.g. Proctor, Forbes & Beasley 2004). Here, the best-fitting stellar population model to a given set of index measurements is found by minimizing the differences between the measured index values and the stellar population model predictions in a χ^2 sense. This approach was already used by our team in Paper VIII, and will be employed for the remainder of this paper to derive the estimates of age, metallicity and abundance ratio for a given set of observed indices. To allow for a reasonable accuracy in the estimates we interpolate the Schiavon models to a fine grid providing 340 681 individual models, spanning $[Z/H] = -1.19$ to 0.57 (in steps of 0.02 dex), age = 0.89 to 17.7 Gyr (logarithmically, in steps of 0.02 dex) and $[\alpha/\text{Fe}] = -0.2$ to 0.5 (in steps of 0.01 dex).⁴ The above model parameter space covers the majority of our measurements for the sample of 48 galaxies. For index measurements which lie outside of the stellar population model parameter space, we use the best-fitting values at the boundary of the interpolated models. However, observed index values are generally covered by the model parameter space and only individual data points may cross the boundaries. We estimate confidence levels on the derived parameters using the $\Delta\chi^2$ values (for details see Press et al. 1992).

We use the χ^2 technique to derive SSP-equivalent stellar population parameters for each bin in our maps. We also use this technique to derive stellar population estimates over circular apertures of one effective radius R_e and of radius $R_e/8$, where all the spectra in these apertures have been summed up and line strength values re-derived. For 28/48 galaxies the SAURON data cover less than one effective radius R_e and we applied aperture corrections to the line strength using the average corrections derived in Paper VI where necessary (see table 4 therein). Corrections for the $H\beta$ index are negligible and are relatively small for the Fe5015 and Mg b indices with maximum corrections of 8 per cent. The fully corrected set of indices is given in Table A1.

Due to our limited wavelength range, only the $H\beta$, Fe5015 and Mg b indices are available for the full field-of-view (FoV). The fourth index, Fe5270_S, typically covers a smaller fraction of the FoV (see Paper VI). However, for a circular aperture of $R_e/8$ we can derive the Fe5270_S values for 37 out of the 48 sample galaxies (see also Table A1). This allows us to compare the stellar population parameters derived by using the Fe5015 index or the more widely utilized Fe5270 index.⁵ The results of the comparison are shown in Fig. 4.

⁴ The Schiavon (2007) models are provided as a function of $[\text{Fe}/\text{H}]$ and were converted by us to $[Z/H]$ as used throughout this paper by a transformation kindly provided by R. Schiavon. As a result of the transformation the models do not cover the full metallicity range given above at each $[\alpha/\text{Fe}]$.

⁵ We convert our Fe5270_S measurements to Fe5270 by using $\text{Fe5270} = 1.26 \times \text{Fe5270}_S + 0.06$ (for details see Kuntschner et al. 2006).

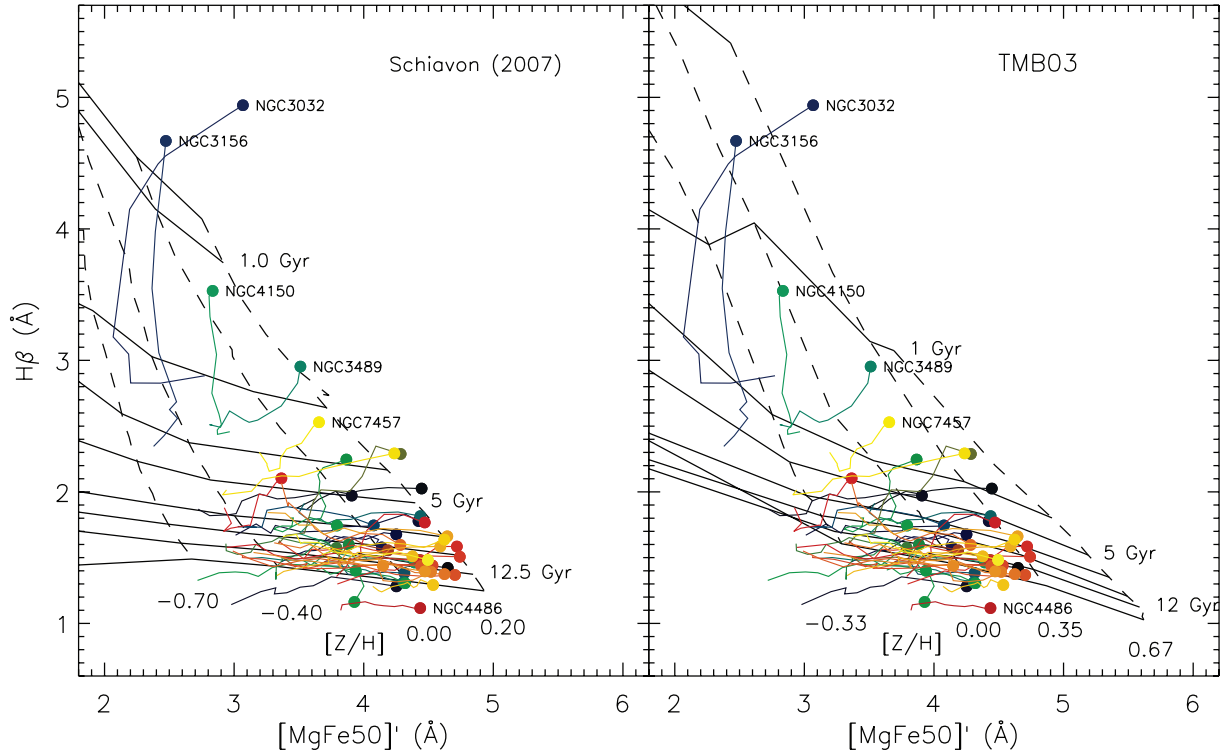


Figure 3. Radial line strength gradients averaged along isophotes for the 48 early-type galaxies in the SAURON sample. The centre of each galaxy is indicated by a filled circle and different colours are used for each galaxy. For galaxies with a strong contribution from a young stellar population ($H\beta > 2.5$ Å), we give the galaxy name next to the central data-point. We also indicate the location of NGC 4486 which exhibits $H\beta$ absorption strength substantially below the models. Overplotted are stellar population models by Schiavon (2007, left) and TMB03 (right) for solar abundance ratios. Note that the TMB03 models extend to $[Z/H] = +0.67$, whereas Schiavon models reach only $[Z/H] = +0.2$.

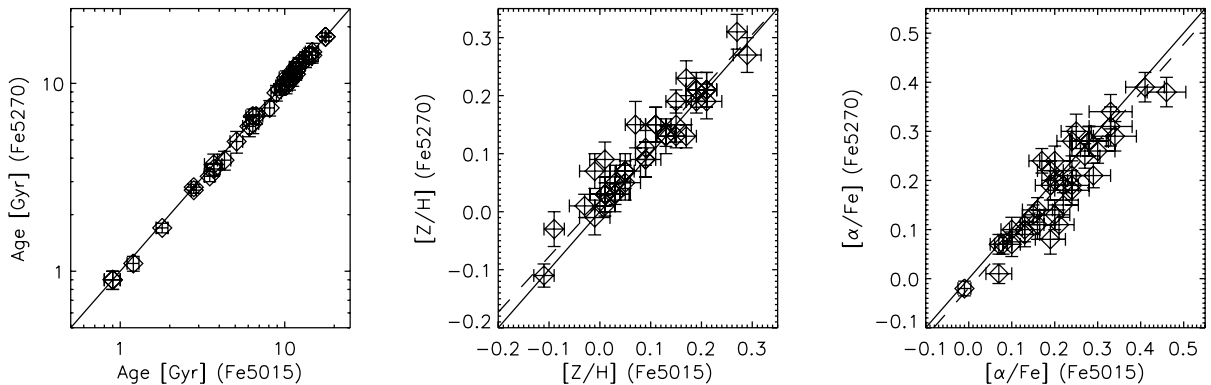


Figure 4. Comparison of stellar population parameters derived from $R_e/8$ circular aperture line strength measurements (see also Table A1) by using the indices $H\beta$, Fe5015 and Mgb or the indices $H\beta$, Mgb and Fe5270 with the χ^2 method and the $[\text{Ti}/\text{Fe}]$ adjusted Schiavon (2007) models as described in Section 3.2. The axis labels indicate which one of the Fe5270 or Fe5015 indices is used. The one-to-one relation is indicated by a solid line in each panel whereas the dashed line shows linear fits to the data taking into account errors in both variables.

Because the $H\beta$ index is the primary age indicator and is used in both derivations, the age estimates show an excellent agreement. Overall, we also find good agreement for the metallicity and abundance ratio estimates with maximum differences of 0.08 dex and 0.11 dex for $[Z/H]$ and $[\alpha/\text{Fe}]$, respectively. Linear fits taking into account errors in both variables are close to the one-to-one relation (see dashed lines in Fig. 4). However, in order to obtain a good agreement for the abundance ratio estimates we used a custom-built version of the Schiavon models (Schiavon, private communication) where $[\text{Ti}/\text{Fe}] = 0.5 \times [\text{Mg}/\text{Fe}]$. More specifically abundance ra-

tios of $[\text{C}/\text{Fe}]$, $[\text{N}/\text{Fe}]$ and $[\text{Cr}/\text{Fe}]$ are fixed to solar ratios, whereas $[\text{O}/\text{Fe}]$, $[\text{Mg}/\text{Fe}]$, $[\text{Ca}/\text{Fe}]$, $[\text{Na}/\text{Fe}]$, $[\text{Si}/\text{Fe}]$ are varied with $[\text{Ti}/\text{Fe}] = 0.5 \times [\text{Mg}/\text{Fe}]$. Using the standard version of the Schiavon models with $[\text{Ti}/\text{Fe}] = [\text{Mg}/\text{Fe}]$ together with the Fe5015 index leads to somewhat underestimated $[\alpha/\text{Fe}]$ ratios for the most massive galaxies. From our data alone, it is not clear whether the Fe5015 index shows a slightly incorrect calibration in the fitting functions or if indeed the $[\text{Ti}/\text{Fe}]$ ratio is not tracking the $[\text{Mg}/\text{Fe}]$ ratio. Further calibrations with e.g. globular cluster data are needed to settle this particular issue. Throughout this paper, we employ the

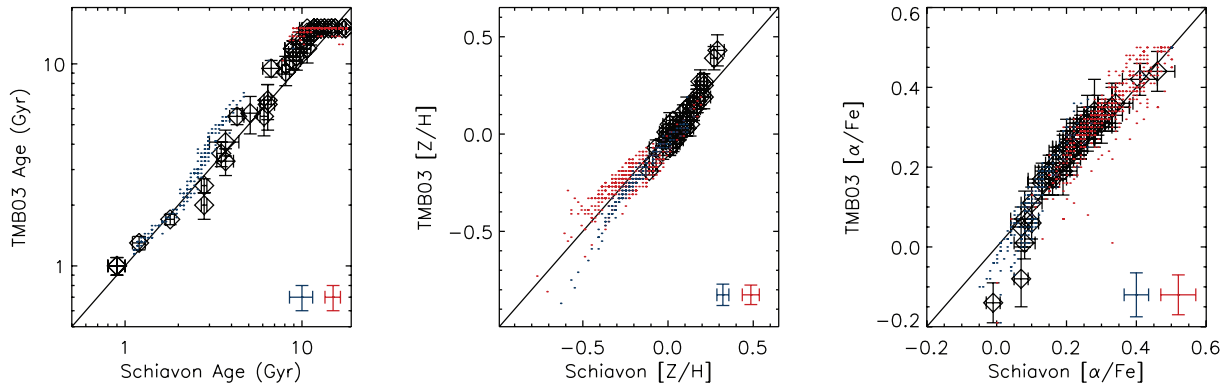


Figure 5. Comparison of stellar population parameters derived from the stellar population models of Schiavon (2007) and TMB03 labelled ‘TMB03’ using the indices $H\beta$, Fe5015 and $Mg\ b$. The black diamonds with error bars represent the $R_e/8$ circular aperture values of our sample of galaxies. The results from the index maps of NGC 4660 and NGC 4150 are shown as red and blue points, respectively. Representative error bars are shown in the lower-right corner of each panel for typical stellar population values for each galaxy.

[Ti/Fe] adjusted models in our estimates of the stellar population parameters.

In Fig. 5, we carry out a comparison of the stellar population parameters derived with our standard set of indices ($H\beta$, Fe5015 and $Mg\ b$) between the Schiavon (2007) and TMB03 models. In order to cover the parameter space probed in this paper, we use the line strength measurements of the $R_e/8$ apertures as well as the index maps of a galaxy with old stellar populations (NGC 4660) and one where young stellar populations dominate (NGC 4150). Overall, we find reasonable to good agreement between the models with the known ‘saturation’ effects of the TMB03 model at old ages (15 Gyr; see also Fig. 3). For estimates of the metallicities $[Z/H]$ and abundance ratios $[\alpha/Fe]$, we find good agreement between the models over a large parameter space. One difference to note though is that for the most metal-rich populations found in the centre of early-type galaxies, the Thomas et al. models predict higher metallicities and younger ages compared to Schiavon. This effect is mainly caused by the different slopes the models predict for $H\beta$ as a function of metallicity (see also Fig. 3). Graves & Schiavon (2008) carry out a more detailed

comparison between the predictions of the Schiavon and Thomas et al. models using the sample of galaxies from Thomas et al. (2005) and also find overall agreement, albeit finding more significant offsets for metallicity and age estimates (see also Smith et al. 2009).

In summary, we conclude that our stellar population estimates derived from $H\beta$, Fe5015 and $Mg\ b$ and the Schiavon models, which we will use for all maps in this paper, agree well with the estimates derived from the more widely used index combination of $H\beta$, $Mg\ b$ and Fe5270 and the predictions from the stellar population models of TMB03.

As the final demonstration of the χ^2 technique, we show in Fig. 6 how the one R_e aperture index values of our sample of 48 early-type galaxies project on to the model grids in planes of $[\alpha/Fe]$ versus $[Z/H]$, $[Z/H]$ versus age and age versus $[\alpha/Fe]$. Error ellipses are drawn for each galaxy and graphically demonstrate the well-known error correlation between $[Z/H]$ and age (e.g. Trager et al. 2000; Kuntschner et al. 2001). In Table 1, we present our estimates of SSP-equivalent age, metallicity and $[\alpha/Fe]$ for circular apertures within $R_e/8$ and one R_e .

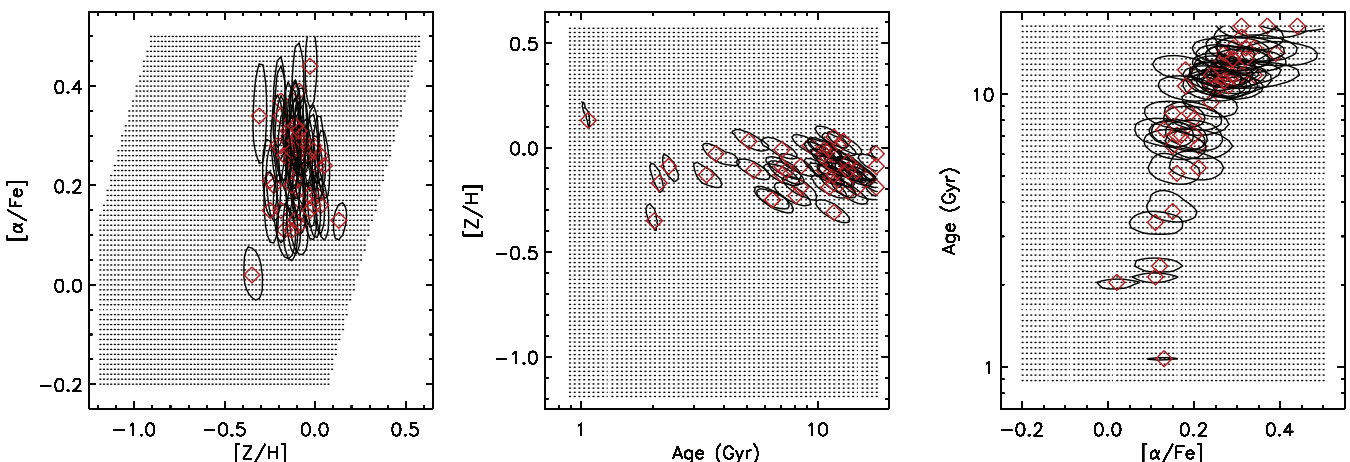


Figure 6. Examples of $\Delta\chi^2$ space for finding the best-fitting stellar population parameters (SSP-equivalent age, metallicity $[Z/H]$ and $[\alpha/Fe]$; Schiavon 2007 models) to the line strengths of all 48 early-type galaxies as measured within a circular aperture of one R_e . The best-fitting model is found by minimizing the difference between the model predictions and the three Lick/IDS indices $H\beta$, Fe5015 and $Mg\ b$. The three panels show different projections of the three-dimensional solution space, with one of the parameters fixed at the best-fitting value. The contours indicate the 1σ confidence levels based on $\Delta\chi^2$ for two degrees of freedom. The small black dots show all grid points where χ^2 is evaluated.

Table 1. List of SSP-equivalent age, metallicity [Z/H] and [α /Fe] estimates within a circular aperture of $R_e/8$ and R_e .

Name	Age (Gyr) $R_e/8$	Metallicity $R_e/8$	[α /Fe] $R_e/8$	Age (Gyr) R_e	Metallicity R_e	[α /Fe] R_e
(1)	(2)	(3)	(4)	(5)	(6)	(7)
NGC 474	$9.3^{+0.4}_{-1.2}$	0.05 ± 0.04	0.16 ± 0.05	$7.1^{+0.7}_{-0.6}$	-0.09 ± 0.04	0.17 ± 0.04
NGC 524	$15.4^{+1.5}_{-1.4}$	0.03 ± 0.04	0.20 ± 0.04	$12.2^{+1.2}_{-1.1}$	0.01 ± 0.04	0.18 ± 0.05
NGC 821	$11.2^{+1.1}_{-1.0}$	0.07 ± 0.02	0.22 ± 0.04	$11.2^{+0.5}_{-1.0}$	-0.13 ± 0.02	0.25 ± 0.04
NGC 1023	$11.7^{+0.6}_{-1.0}$	0.09 ± 0.02	0.19 ± 0.04	$11.7^{+1.7}_{-0.5}$	-0.03 ± 0.04	0.26 ± 0.04
NGC 2549	$3.7^{+0.4}_{-0.3}$	0.27 ± 0.02	0.15 ± 0.03	$5.1^{+0.5}_{-0.2}$	0.03 ± 0.02	0.16 ± 0.04
NGC 2685	$5.1^{+0.5}_{-0.4}$	-0.01 ± 0.04	0.19 ± 0.04	$6.4^{+1.0}_{-0.6}$	-0.25 ± 0.04	0.21 ± 0.05
NGC 2695	$16.9^{+0.8}_{-1.5}$	-0.01 ± 0.04	0.31 ± 0.05	$17.7^{+0.1}_{-0.8}$	-0.19 ± 0.02	0.37 ± 0.06
NGC 2699	$6.4^{+0.6}_{-0.6}$	0.21 ± 0.02	0.16 ± 0.04	$8.5^{+0.4}_{-1.1}$	-0.09 ± 0.04	0.19 ± 0.05
NGC 2768	$8.9^{+0.9}_{-0.8}$	0.01 ± 0.04	0.26 ± 0.04	$11.2^{+1.1}_{-1.0}$	-0.19 ± 0.02	0.28 ± 0.06
NGC 2974	$8.9^{+0.9}_{-0.4}$	0.11 ± 0.04	0.29 ± 0.04	$9.3^{+0.9}_{-0.8}$	0.01 ± 0.02	0.24 ± 0.04
NGC 3032	$0.9^{+0.1}_{-0.1}$	0.03 ± 0.04	0.07 ± 0.02	$1.1^{+0.1}_{-0.1}$	0.13 ± 0.06	0.13 ± 0.02
NGC 3156	$0.9^{+0.1}_{-0.1}$	0.05 ± 0.02	-0.01 ± 0.02	$2.0^{+0.1}_{-0.1}$	-0.35 ± 0.06	0.02 ± 0.04
NGC 3377	$6.7^{+0.7}_{-0.6}$	0.01 ± 0.04	0.24 ± 0.04	$8.1^{+0.4}_{-1.0}$	-0.23 ± 0.04	0.20 ± 0.05
NGC 3379	$14.7^{+0.7}_{-1.9}$	0.01 ± 0.04	0.28 ± 0.05	$14.7^{+1.4}_{-1.3}$	-0.11 ± 0.02	0.29 ± 0.05
NGC 3384	$6.1^{+0.3}_{-0.8}$	0.19 ± 0.02	0.13 ± 0.04	$7.1^{+0.7}_{-0.6}$	-0.01 ± 0.04	0.16 ± 0.04
NGC 3414	$13.4^{+1.3}_{-1.2}$	0.03 ± 0.04	0.34 ± 0.05	$13.4^{+1.3}_{-1.2}$	-0.21 ± 0.04	0.28 ± 0.06
NGC 3489	$1.8^{+0.1}_{-0.2}$	0.15 ± 0.02	0.10 ± 0.02	$2.3^{+0.1}_{-0.1}$	-0.09 ± 0.04	0.12 ± 0.03
NGC 3608	$11.7^{+0.6}_{-1.0}$	0.05 ± 0.04	0.24 ± 0.04	$10.7^{+0.5}_{-0.9}$	-0.11 ± 0.02	0.24 ± 0.04
NGC 4150	$1.2^{+0.1}_{-0.1}$	0.07 ± 0.02	0.08 ± 0.03	$2.1^{+0.1}_{-0.1}$	-0.17 ± 0.06	0.11 ± 0.04
NGC 4262	$14.1^{+1.4}_{-1.2}$	-0.01 ± 0.04	0.33 ± 0.05	$14.7^{+1.4}_{-1.3}$	-0.19 ± 0.04	0.34 ± 0.06
NGC 4270	$8.1^{+0.4}_{-1.0}$	-0.07 ± 0.04	0.08 ± 0.04	$8.5^{+0.8}_{-0.7}$	-0.19 ± 0.04	0.15 ± 0.05
NGC 4278	$17.7^{+0.1}_{-1.6}$	0.01 ± 0.02	0.46 ± 0.05	$14.1^{+1.4}_{-1.2}$	-0.09 ± 0.04	0.39 ± 0.06
NGC 4374	$14.7^{+1.4}_{-1.3}$	0.01 ± 0.04	0.30 ± 0.04	$16.1^{+1.6}_{-2.1}$	-0.15 ± 0.04	0.31 ± 0.06
NGC 4382	$3.7^{+0.7}_{-0.2}$	0.05 ± 0.04	0.16 ± 0.04	$5.4^{+0.5}_{-0.5}$	-0.11 ± 0.04	0.21 ± 0.04
NGC 4387	$10.2^{+0.5}_{-1.3}$	-0.03 ± 0.04	0.20 ± 0.04	$11.7^{+1.7}_{-0.5}$	-0.17 ± 0.04	0.26 ± 0.06
NGC 4458	$10.7^{+1.0}_{-0.9}$	-0.11 ± 0.02	0.28 ± 0.05	$11.7^{+1.1}_{-1.0}$	-0.31 ± 0.04	0.34 ± 0.06
NGC 4459	$3.5^{+0.2}_{-0.3}$	0.17 ± 0.02	0.22 ± 0.04	$7.1^{+0.7}_{-0.6}$	-0.13 ± 0.02	0.20 ± 0.04
NGC 4473	$11.7^{+0.6}_{-1.0}$	0.09 ± 0.02	0.24 ± 0.04	$12.2^{+1.8}_{-0.6}$	-0.09 ± 0.04	0.27 ± 0.04
NGC 4477	$9.7^{+0.9}_{-0.9}$	0.03 ± 0.04	0.24 ± 0.04	$11.7^{+1.1}_{-1.0}$	-0.13 ± 0.02	0.26 ± 0.04
NGC 4486	$17.7^{+0.1}_{-0.1}$	0.13 ± 0.02	0.41 ± 0.05	$17.7^{+0.1}_{-0.1}$	-0.03 ± 0.02	0.44 ± 0.05
NGC 4526	$6.4^{+0.3}_{-0.8}$	0.19 ± 0.02	0.22 ± 0.04	$10.7^{+1.0}_{-0.9}$	-0.01 ± 0.02	0.28 ± 0.05
NGC 4546	$10.7^{+1.0}_{-0.9}$	0.13 ± 0.02	0.27 ± 0.04	$11.7^{+1.1}_{-1.0}$	-0.13 ± 0.02	0.31 ± 0.05
NGC 4550	$4.3^{+0.4}_{-0.4}$	-0.09 ± 0.02	0.21 ± 0.04	$6.4^{+0.6}_{-0.8}$	-0.25 ± 0.04	0.15 ± 0.05
NGC 4552	$10.2^{+1.0}_{-0.9}$	0.21 ± 0.04	0.25 ± 0.04	$12.8^{+1.2}_{-1.1}$	0.03 ± 0.04	0.26 ± 0.05
NGC 4564	$10.7^{+0.5}_{-0.9}$	0.21 ± 0.02	0.19 ± 0.03	$10.7^{+1.6}_{-0.5}$	-0.05 ± 0.04	0.26 ± 0.04
NGC 4570	$11.7^{+1.1}_{-1.0}$	0.17 ± 0.02	0.17 ± 0.03	$14.1^{+1.4}_{-1.2}$	-0.13 ± 0.04	0.27 ± 0.04
NGC 4621	$13.4^{+1.3}_{-1.2}$	0.09 ± 0.04	0.28 ± 0.05	$14.7^{+0.7}_{-1.9}$	-0.11 ± 0.04	0.32 ± 0.06
NGC 4660	$12.2^{+1.2}_{-0.6}$	0.15 ± 0.02	0.24 ± 0.04	$13.4^{+1.3}_{-1.2}$	-0.11 ± 0.02	0.29 ± 0.05
NGC 5198	$12.2^{+1.2}_{-1.1}$	0.13 ± 0.04	0.26 ± 0.04	$11.7^{+1.1}_{-1.0}$	-0.09 ± 0.02	0.29 ± 0.04
NGC 5308	$12.8^{+0.6}_{-1.1}$	0.05 ± 0.04	0.24 ± 0.04	$13.4^{+1.3}_{-1.2}$	-0.07 ± 0.04	0.29 ± 0.05
NGC 5813	$11.7^{+1.7}_{-0.5}$	0.05 ± 0.04	0.33 ± 0.05	$13.4^{+0.6}_{-1.7}$	-0.11 ± 0.04	0.32 ± 0.06
NGC 5831	$8.1^{+0.4}_{-0.7}$	0.11 ± 0.02	0.13 ± 0.04	$7.4^{+0.7}_{-0.7}$	-0.11 ± 0.04	0.13 ± 0.04
NGC 5838	$9.3^{+0.9}_{-0.4}$	0.19 ± 0.02	0.20 ± 0.03	$11.2^{+0.5}_{-1.4}$	-0.01 ± 0.04	0.27 ± 0.04
NGC 5845	$11.2^{+0.5}_{-1.0}$	0.15 ± 0.04	0.20 ± 0.04	$11.7^{+0.6}_{-1.0}$	0.05 ± 0.02	0.24 ± 0.04
NGC 5846	$15.4^{+0.7}_{-1.4}$	0.09 ± 0.02	0.28 ± 0.04	$17.7^{+0.1}_{-1.6}$	-0.09 ± 0.04	0.31 ± 0.05
NGC 5982	$8.9^{+0.9}_{-0.8}$	0.17 ± 0.02	0.15 ± 0.03	$10.7^{+0.5}_{-0.9}$	-0.03 ± 0.02	0.18 ± 0.04
NGC 7332	$2.8^{+0.1}_{-0.1}$	0.29 ± 0.04	0.10 ± 0.03	$3.7^{+0.5}_{-0.2}$	-0.03 ± 0.02	0.15 ± 0.04
NGC 7457	$2.8^{+0.1}_{-0.1}$	0.01 ± 0.04	0.07 ± 0.03	$3.4^{+0.2}_{-0.3}$	-0.13 ± 0.04	0.11 ± 0.04

Notes. (1) NGC number. (2)–(4) SSP-equivalent estimates of age, metallicity [Z/H] and [α /Fe] within a circular aperture of $R_e/8$. (5)–(7) SSP-equivalent estimates of age, metallicity [Z/H] and [α /Fe] within a circular aperture of one R_e . For galaxies with less than one R_e coverage we applied the aperture corrections given in Paper VI to the line strength indices and then derived the stellar population estimates.

3.3 Interpretation of derived stellar population parameters

A word of caution is necessary when making use of the stellar population models described above to interpret the observed line strength indices. Each of the stellar population models for a given age, metallicity and abundance ratio is made of a set of stars that all have the same age, metallicity and abundance ratio. Strictly speaking, these models can then only be applied to objects, or specific regions within objects for which this is also true. Since we observe the integrated light along the line-of-sight for our target galaxies we clearly violate this condition even if only metallicity gradients are considered. The problem is even larger for galaxies with signs of multiple star formation periods. In practice, the derived stellar parameters, from any of the methods described above, are interpreted as *SSP-equivalent*. Serra & Trager (2007) investigated the SSP-equivalent age and chemical composition measured from Lick/IDS line strength indices of a large set of two-population (old plus young), composite model stellar populations. Their conclusions are that SSP-equivalent estimates are biased such that the derived SSP age depends primarily on the age of the young population, while the derived SSP chemical composition is weighted more towards that of the old population. Furthermore, in this context, the age of a young stellar component and the mass fraction between old and young stars are degenerate.

Changes in observed line strength measurements due to interstellar extinction, most likely to be present for early-type galaxies with signs of recent star formation, are negligible. Basic simulations show that with a standard extinction curve (Fitzpatrick 1999) and $E(B - V) = 0.7$, the $H\beta$, Fe5015, Mg *b* and Fe5270 indices change by less than 0.01, 0.05, 0.01 and 0.02 Å, respectively, compared to the dust-free models.

Given the biases and degeneracies described above, we find that the broad conclusions on the ages and chemical composition of our sample as described here are still valid, but individual determinations for a given spectrum can be biased in the presence of composite stellar populations. Specifically, the SSP-equivalent age estimate is strongly biased towards the last star formation event rather than tracing the age of the majority of the stars contributing to the integrated spectrum.

4 RESULTS

Figs 7(a)–(l) present maps of SSP-equivalent age, metallicity [Z/H] and abundance ratio [α /Fe] of the 48 early-type galaxies in the SAURON sample, ordered by increasing NGC number. For each galaxy, we show the total intensity reconstructed from the full wavelength range of the SAURON spectra (see also Paper III), and the two-dimensional distributions of age, [Z/H] and [α /Fe] overplotted with isophotes of the reconstructed image spaced by single magnitude steps. We also include the stellar velocity maps previously shown in Paper III⁶ in the bottom panel for each galaxy, used as reference for our discussion. The maps are all plotted with the same spatial scale, and oriented with respect to the SAURON field for presentation purposes. The relative directions of north and east are indicated by the orientation arrow next to the galaxy title. The maximum and minimum of the plotting range is given in the tab attached

⁶ The kinematics were re-derived using the new stellar template library as described in Section 2. However, there are only very minor ($\Delta v \leq 10 \text{ km s}^{-1}$) changes in the recession velocities, thus the visual impression of the maps is identical to Paper III.

to each parameter map, and the colour bar indicates the colour table used. In order to allow for an easy comparison between galaxies, the plotting range of the age maps is fixed to the range 0.4 to 18 Gyr, where the colour bars reflect a linear scaling. The colours are adjusted such that blue to dark-green shades correspond to old stellar populations (10–18 Gyr), while younger stellar populations are represented by red and yellow shades. Similarly, the plotting range of the [α /Fe] maps is fixed to the range -0.2 to $+0.5$ for all galaxies. For the [Z/H] maps we use an independent plotting range for each galaxy in order to better visualize the metallicity distribution across the FoV.

In Paper VI, we found non-physical values of the $H\beta$, Fe5015 and Mg *b* line strengths in the outer regions of some galaxies where many individual lenslets are averaged to achieve the target S/N of 60. Additionally, we removed regions where an SSP interpretation is not meaningful; for example the central AGN-contaminated region and the jet of NGC 4486 or the regions affected by neighbour galaxies of NGC 5846 and the regions affected by foreground stars. These bins are indicated with grey colour in the maps presented in Figs 7(a)–(l).

Whenever we make reference to the dynamical mass of a galaxy, we have estimated it with the scalar virial relation

$$M_{\text{dyn}} = 5.0 \times R_e \sigma_e^2 / G, \quad (3)$$

where σ_e is the luminosity-weighted second velocity moment within one effective (half-light) radius R_e and the factor of 5.0 was calibrated using detailed dynamical models in Paper IV. This mass represents

$$M_{\text{dyn}} \approx 2 \times M_{1/2}, \quad (4)$$

where $M_{1/2}$ is the total dynamical mass within a sphere containing half of the galaxy light. It should not be confused with the much larger total galaxy mass within the virial radius.

4.1 Overview of stellar population maps

The stellar population maps in Figs 7(a)–(l) show a wealth of structures. Some general trends are apparent and we discuss these in the following.

4.1.1 Age maps

To aid the discussion in this section and to provide a simple overview of the different age map categories, we show in Fig. 8 radial line strength gradients averaged along isophotes with the predictions of stellar population models overplotted. This is similar to Fig. 3. However, here we have separated the galaxies into four groups according to their radial age gradients. For each galaxy we indicate by colour whether it belongs to the fast rotators (blue) or slow rotators (red; see Paper IX). An overview of the various star formation indicators used in the SAURON survey is given in Table 2, where galaxies have been grouped in the same manner as in Fig. 8.

About 60 per cent of the 48 galaxies in our sample show roughly flat age maps of dark-blue to green colour indicating an overall old age (≥ 9 Gyr) over the observed FoV. Due to the linear sampling of the colour map in age, the similar colour in our maps hides potentially significant age variations in absolute terms (9–18 Gyr). This reflects, however, the increased error in our age estimates towards older ages, which is dictated by the age sensitivity of the $H\beta$ index, becoming more uncertain for the same index measurement error at older ages (see also Fig. 3).

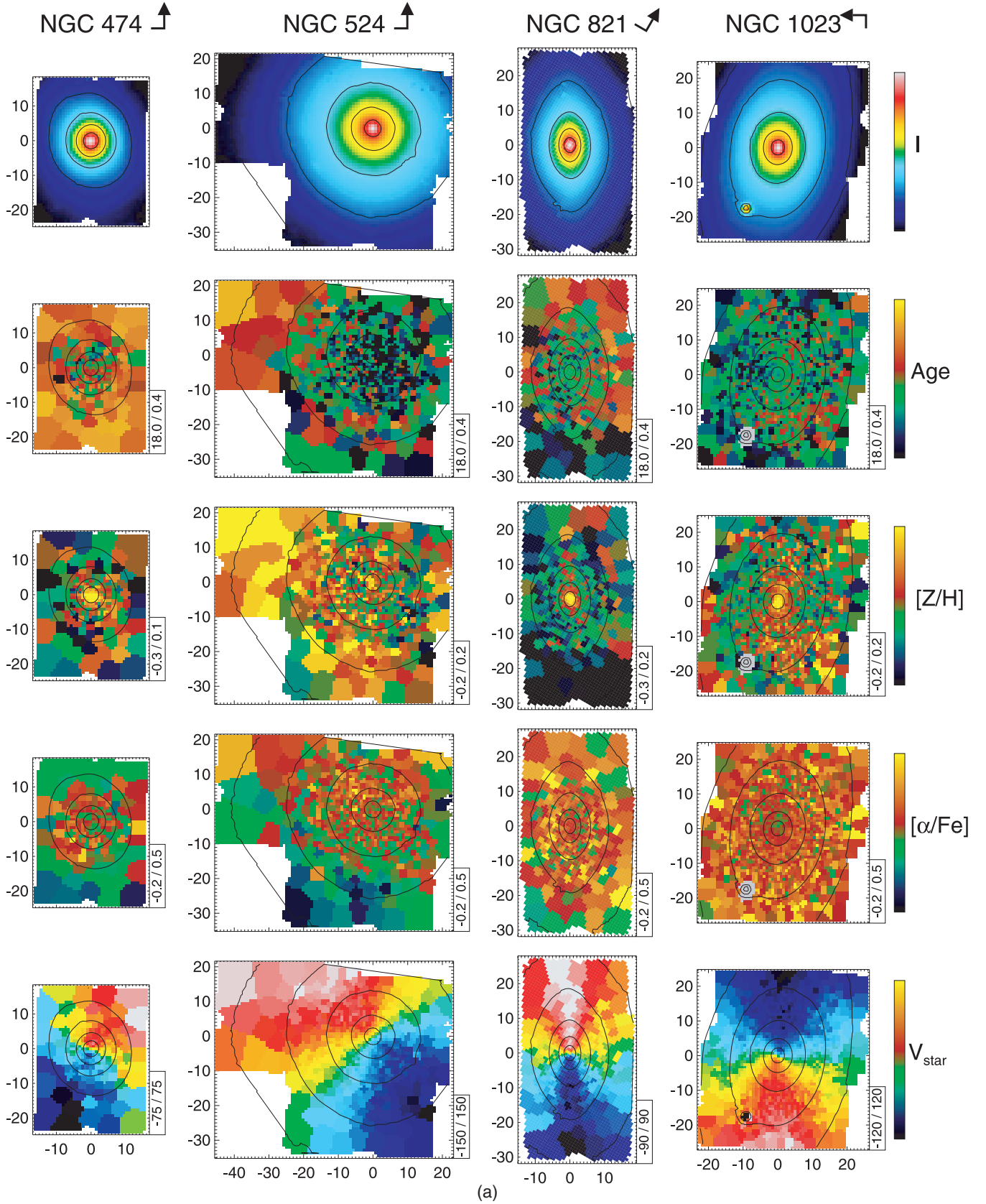


Figure 7. Maps of the derived stellar populations of the 48 early-type galaxies in the SAURON representative sample. The SAURON spectra have been spatially binned to a minimum S/N of 40 by means of the centroidal Voronoi tessellation algorithm of Cappellari & Copin (2003). All maps have the same spatial scale and the units of x- and y-axis are arcsec. From top to bottom: (i) reconstructed total intensity; (ii) SSP-equivalent age distribution (the age scale is given in units of Gyr and a linear colour scale); (iii) metallicity ($[Z/H]$) distribution and (iv) $[\alpha/Fe]$ distribution. The bottom panel in each column reproduces the velocity maps from Paper III.

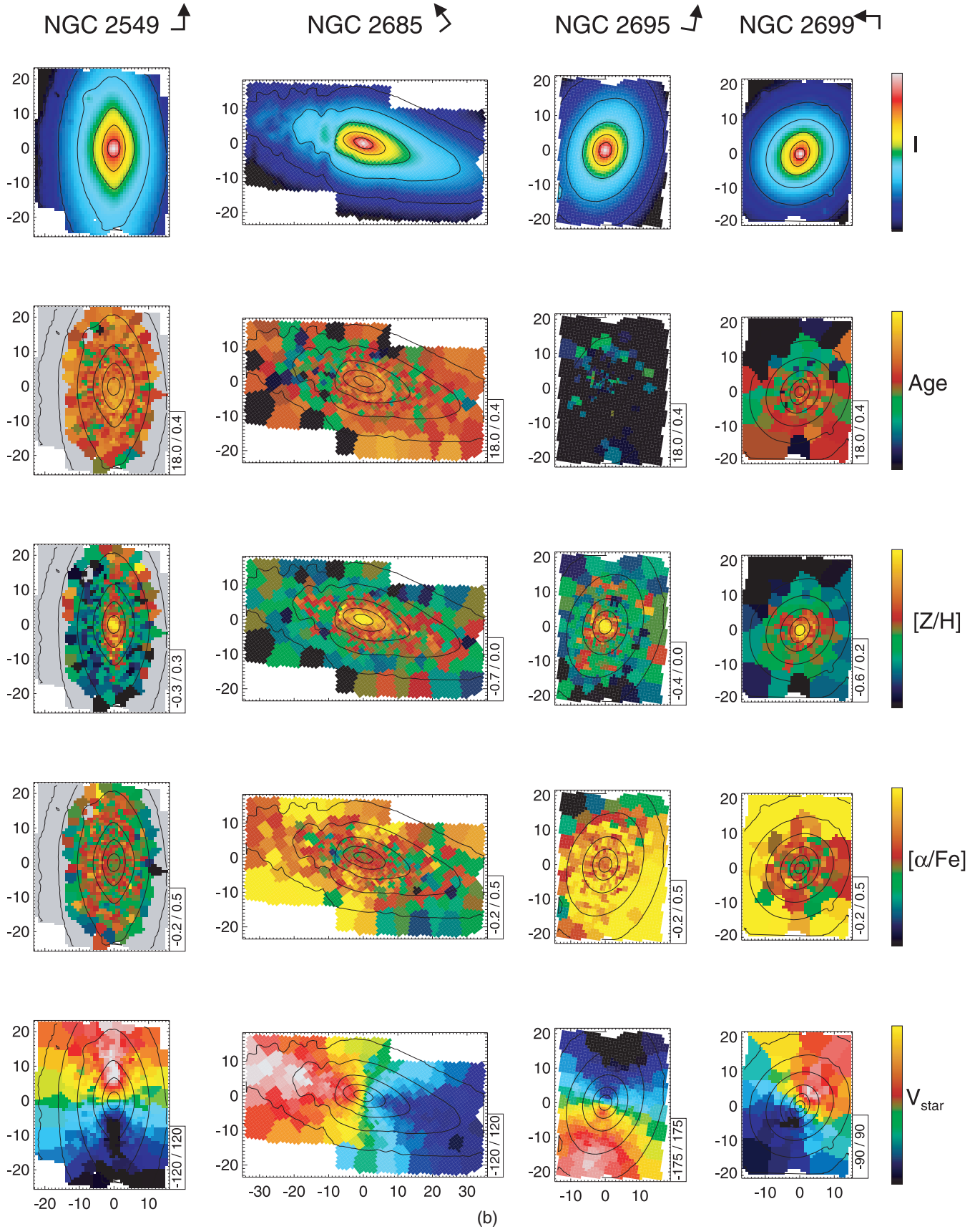
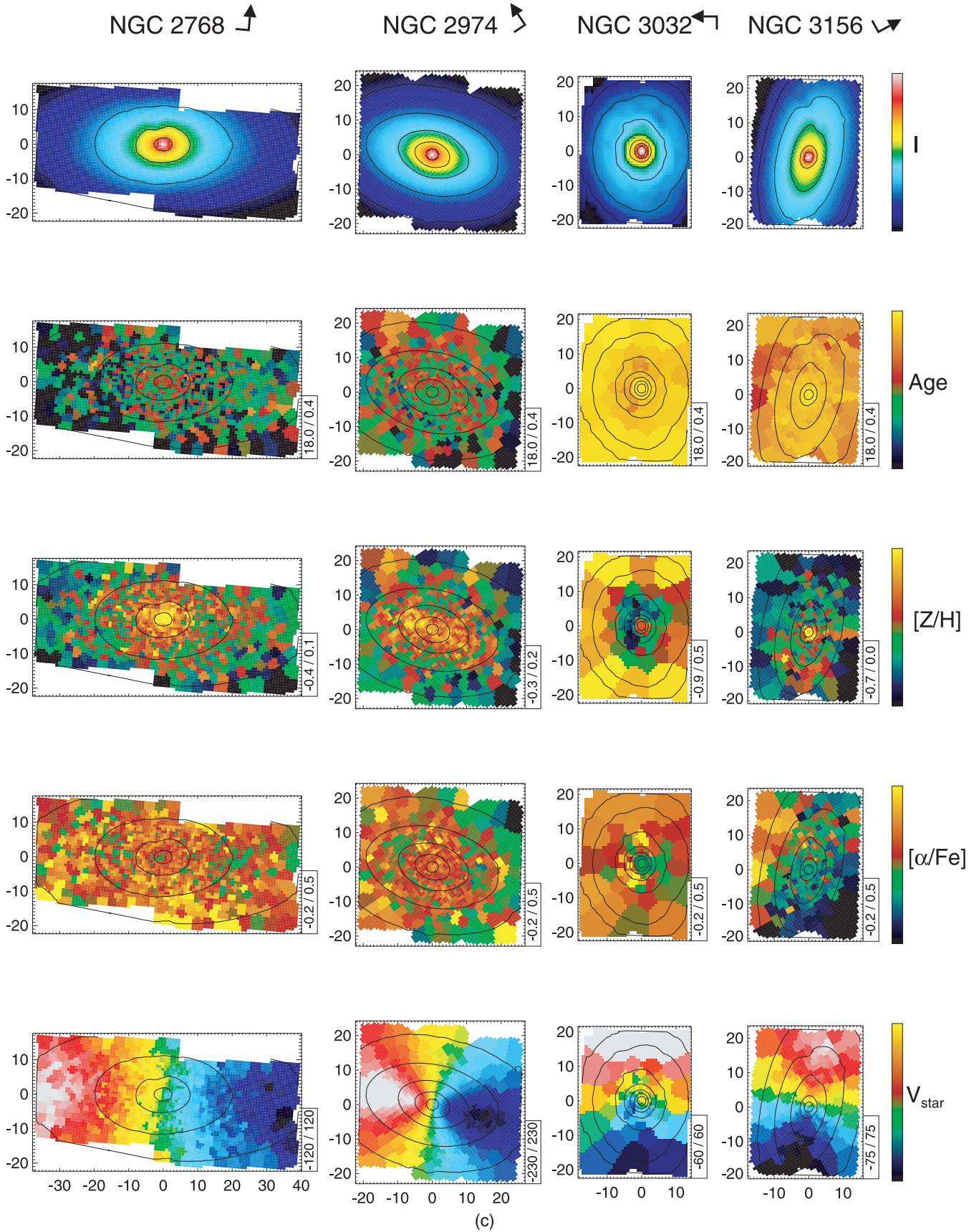


Figure 7 – continued



(c)

Figure 7 – continued

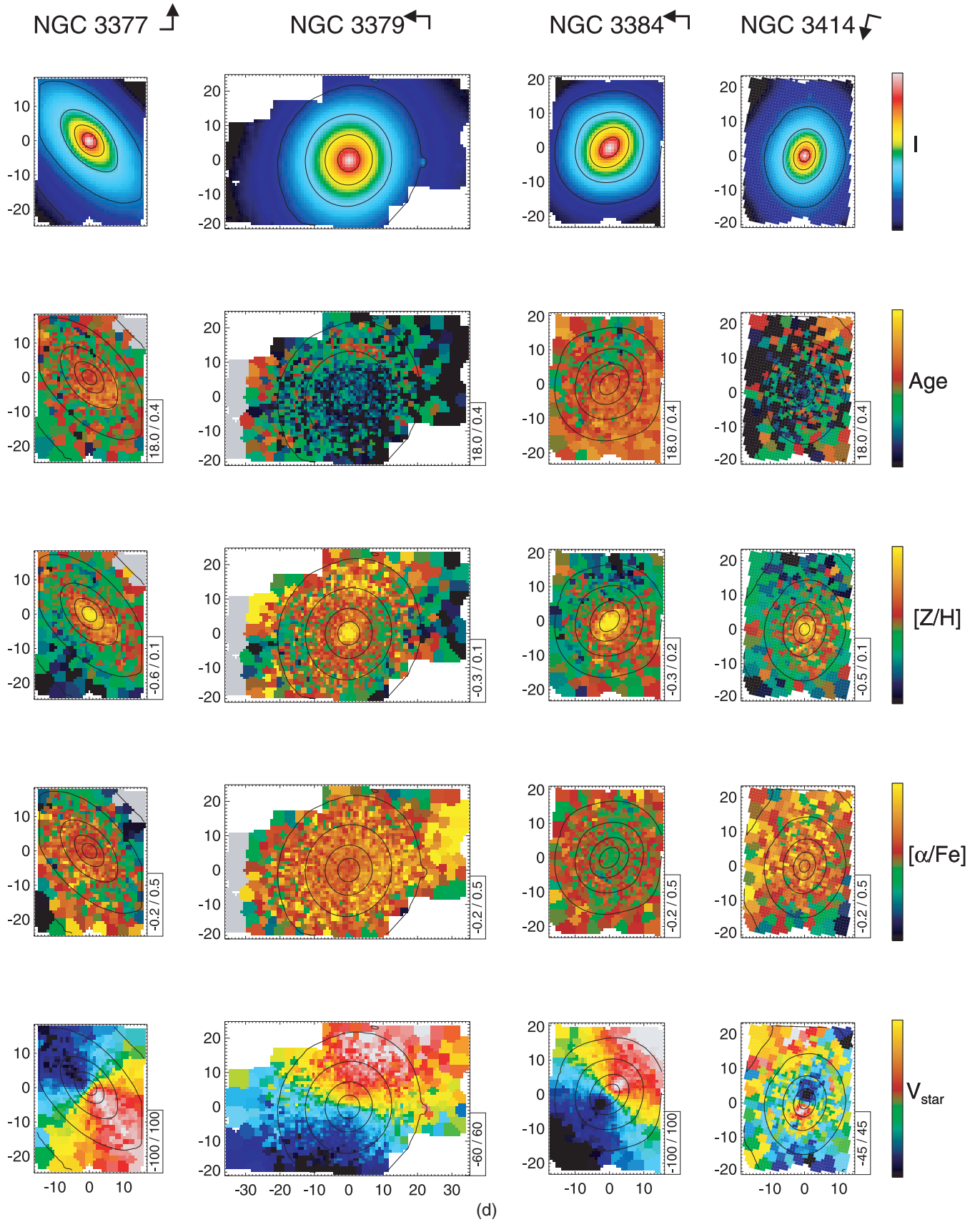
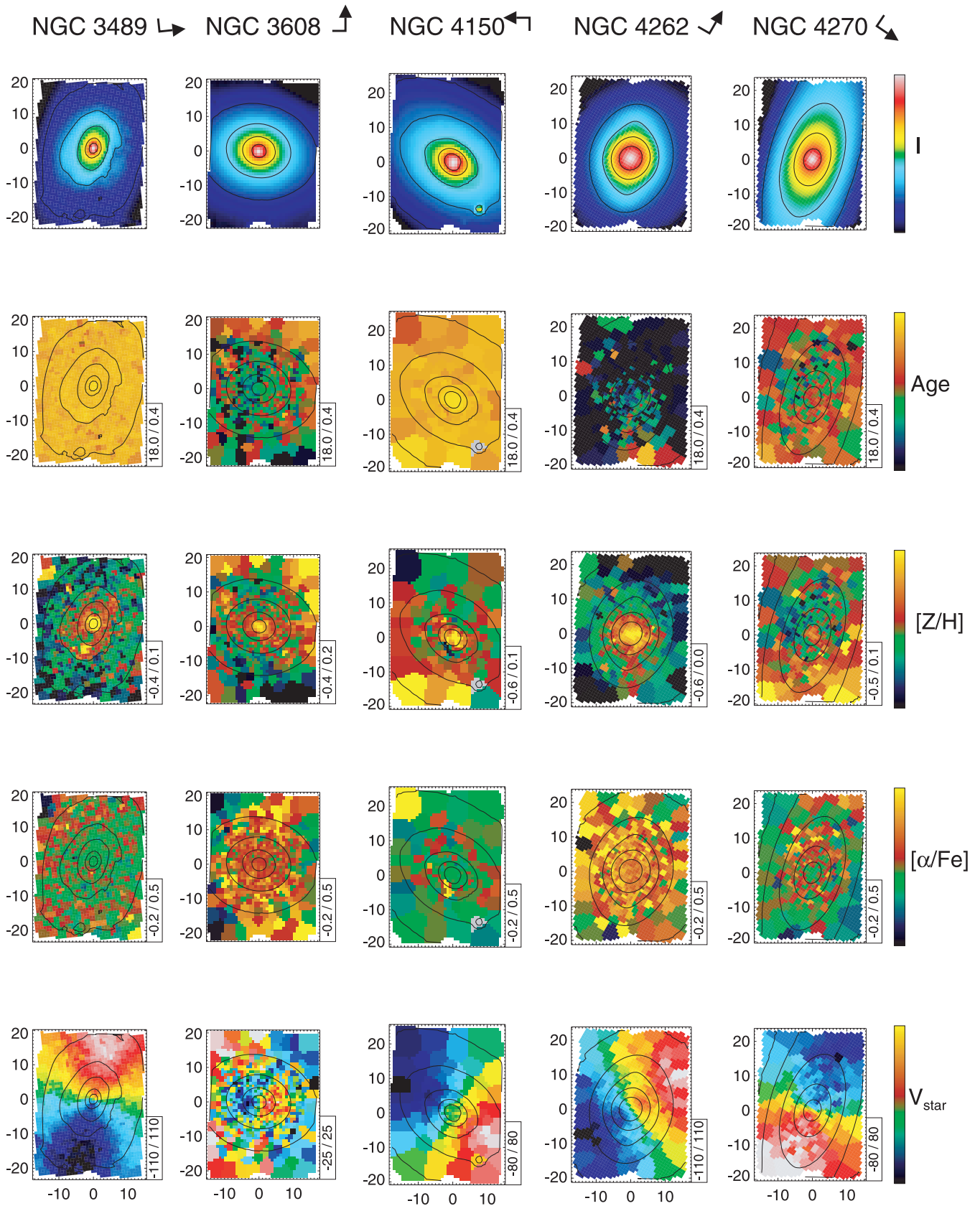


Figure 7 – continued



(e)

Figure 7 – continued

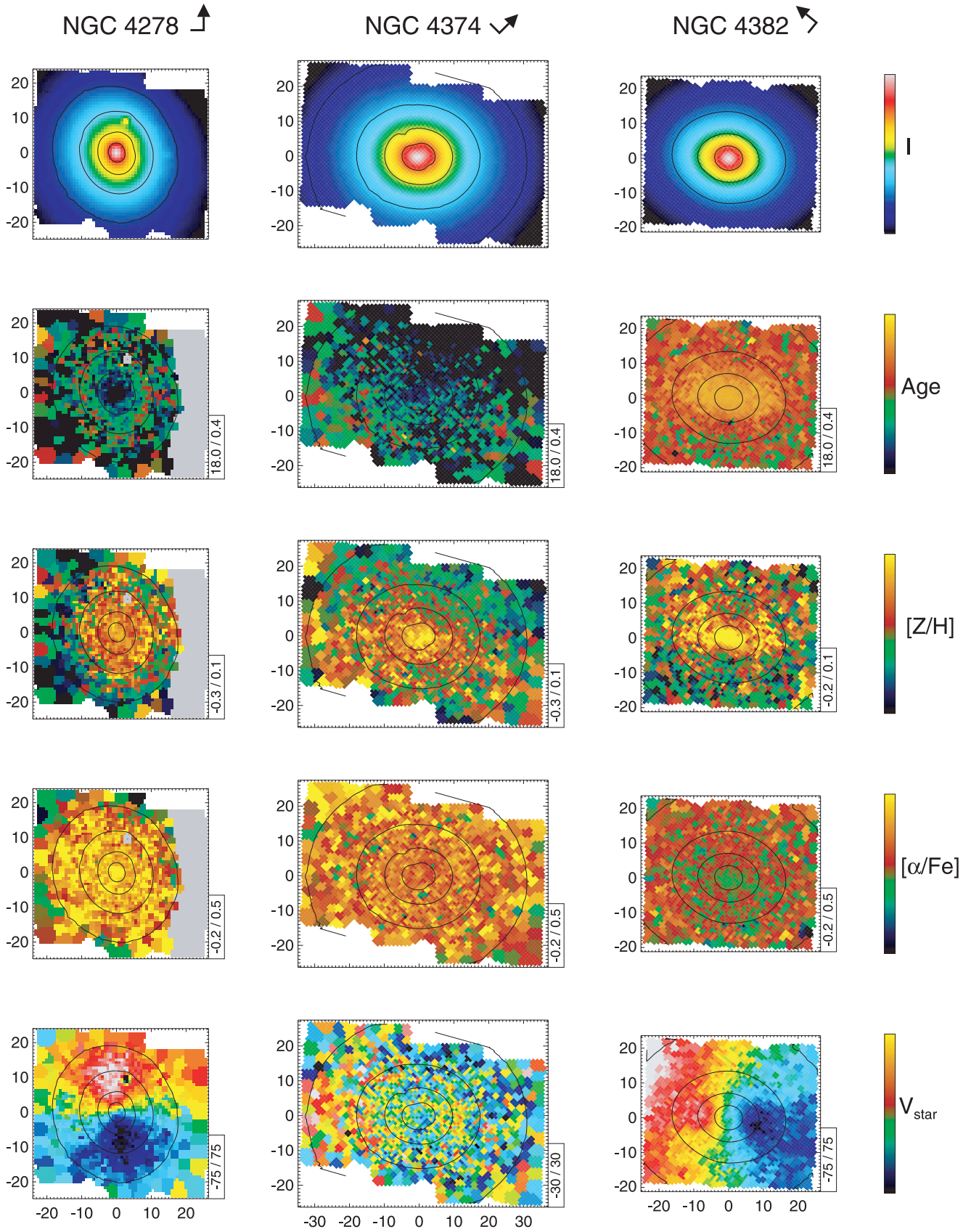


Figure 7 – continued

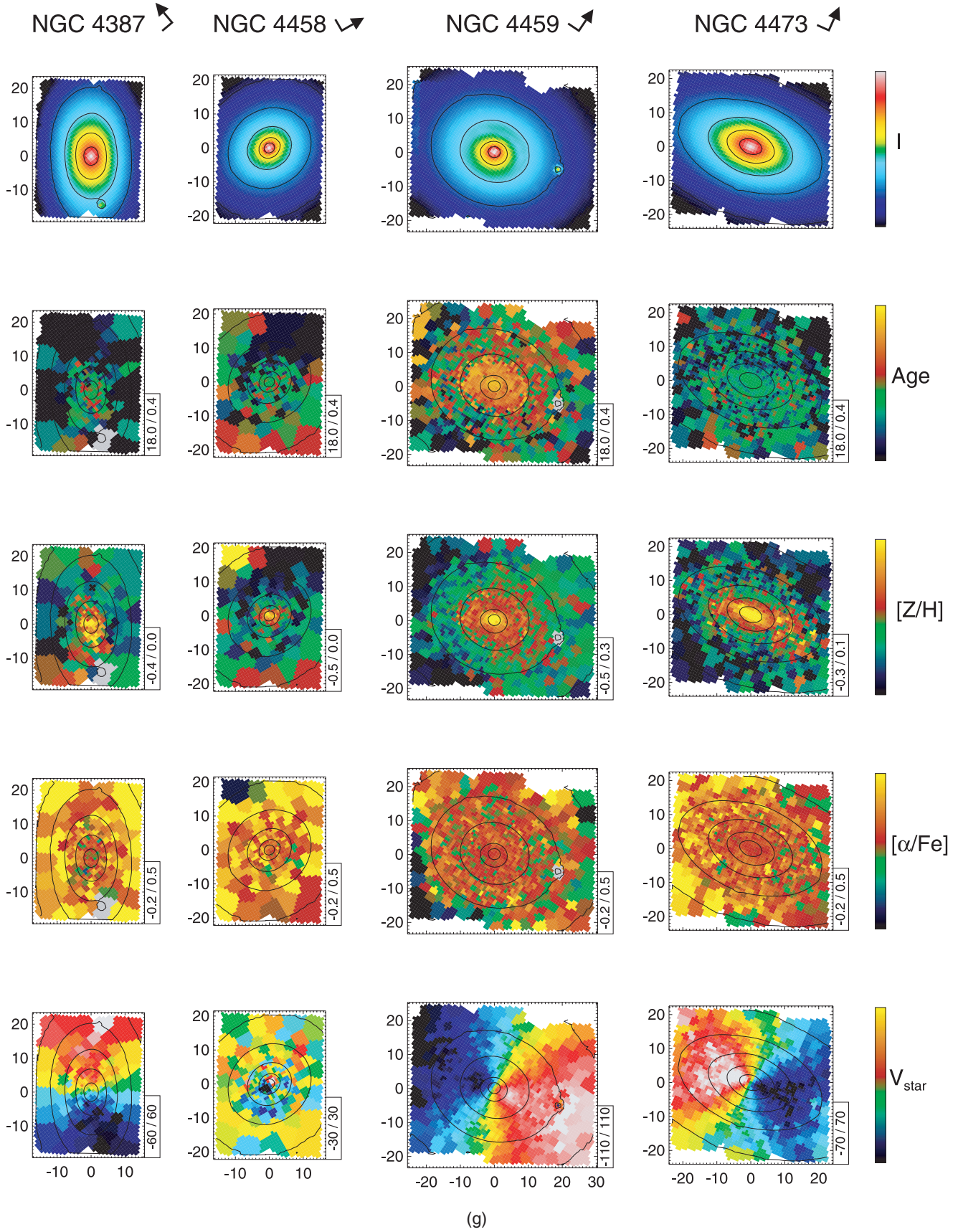


Figure 7 – continued

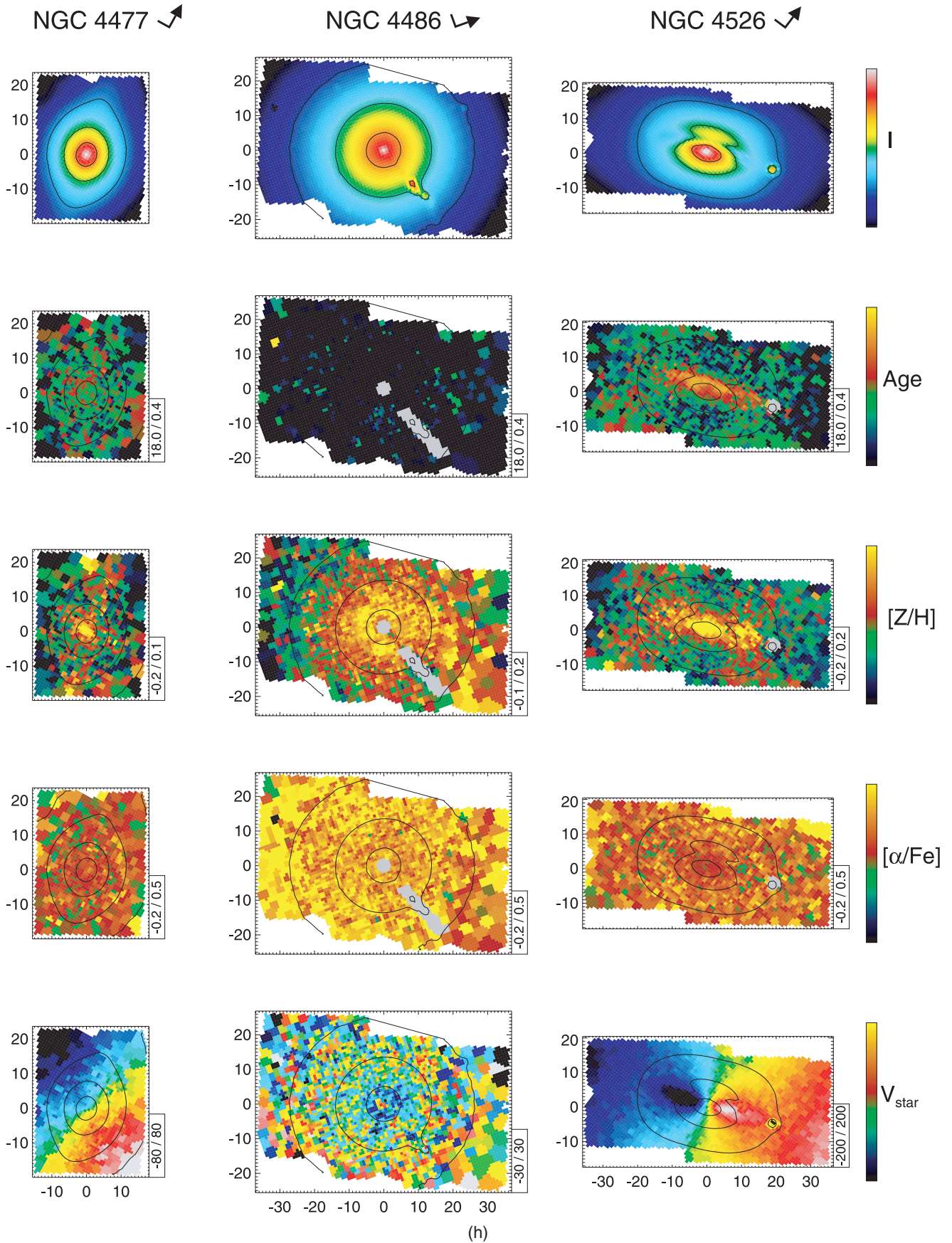


Figure 7 – continued

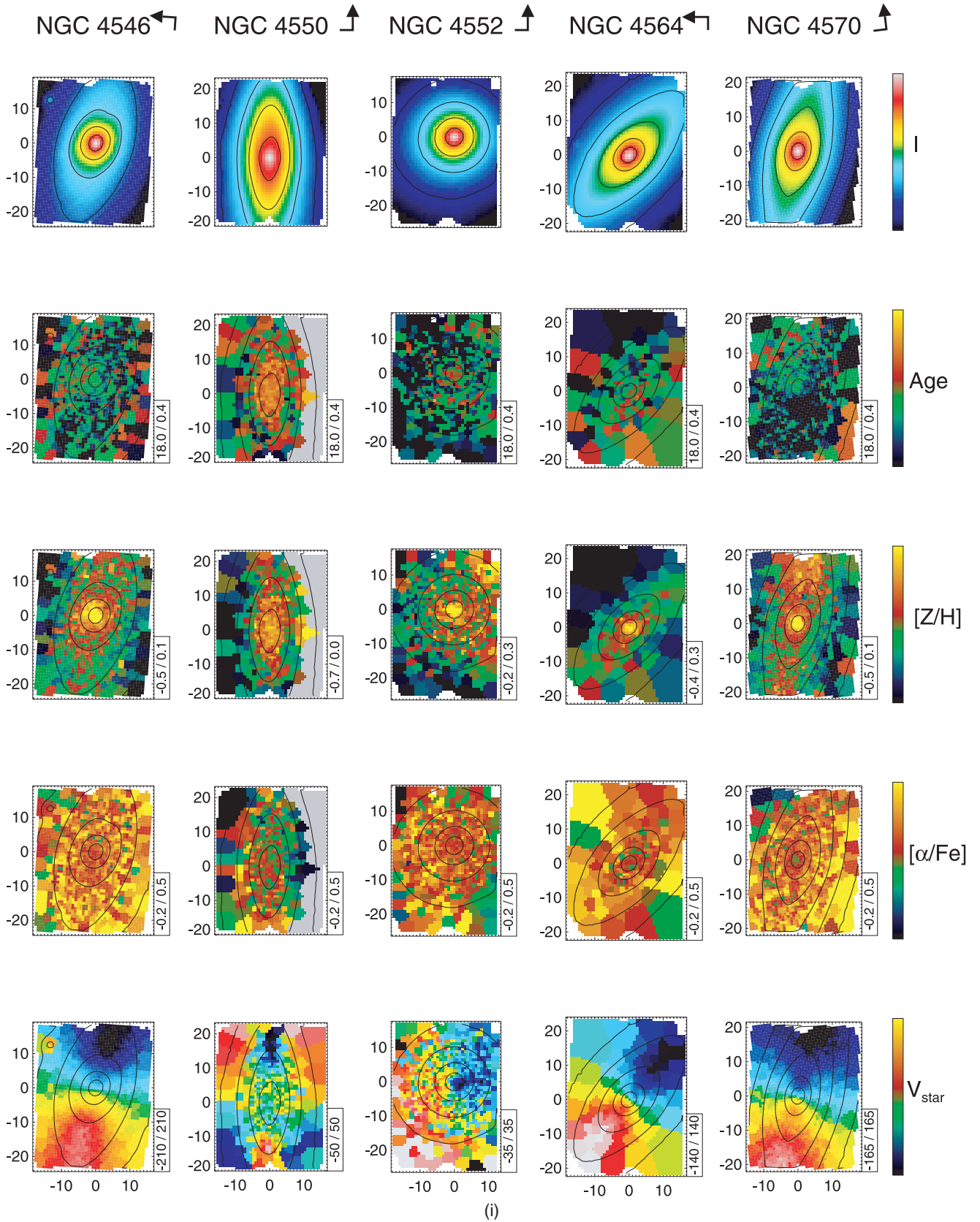


Figure 7 – continued

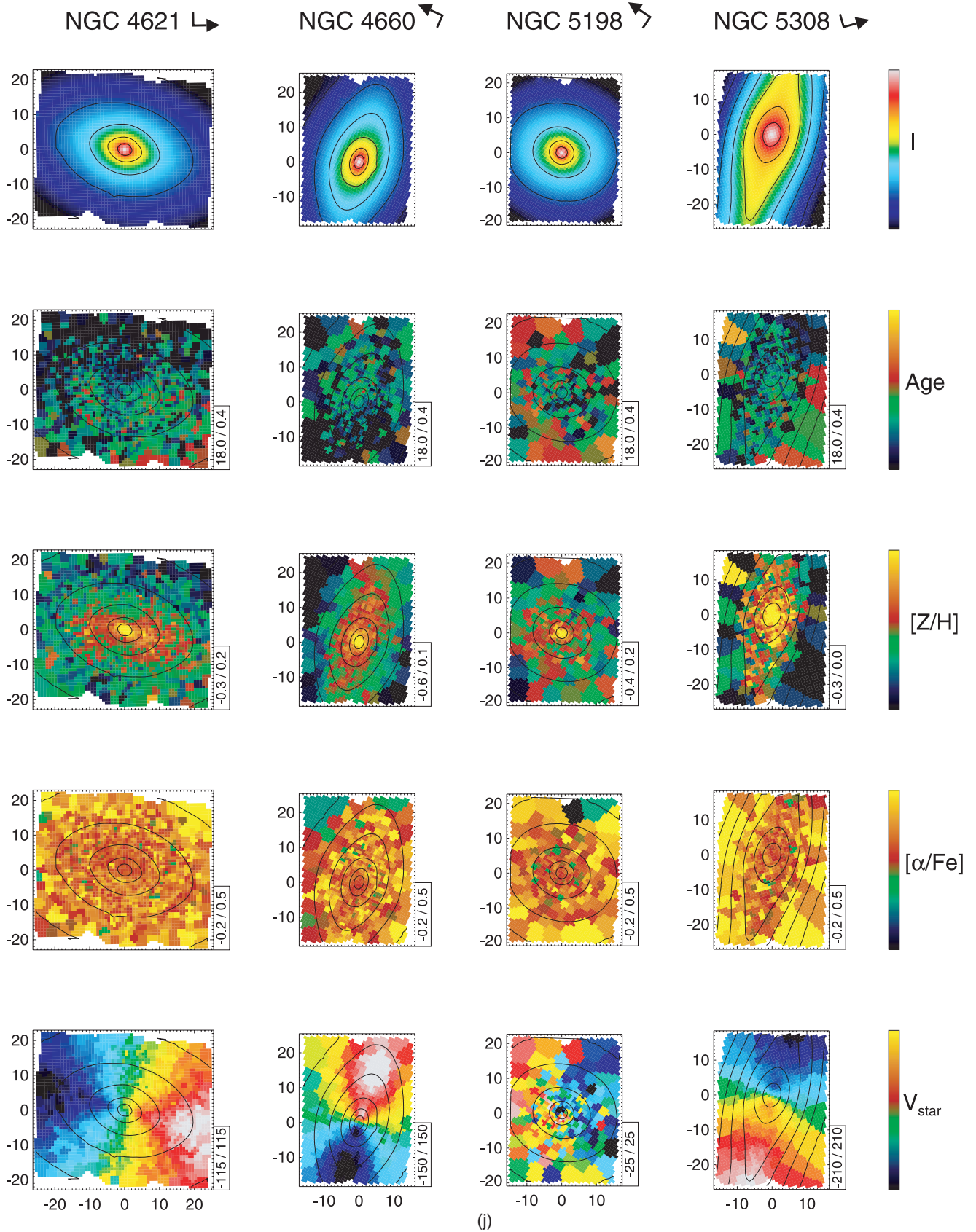
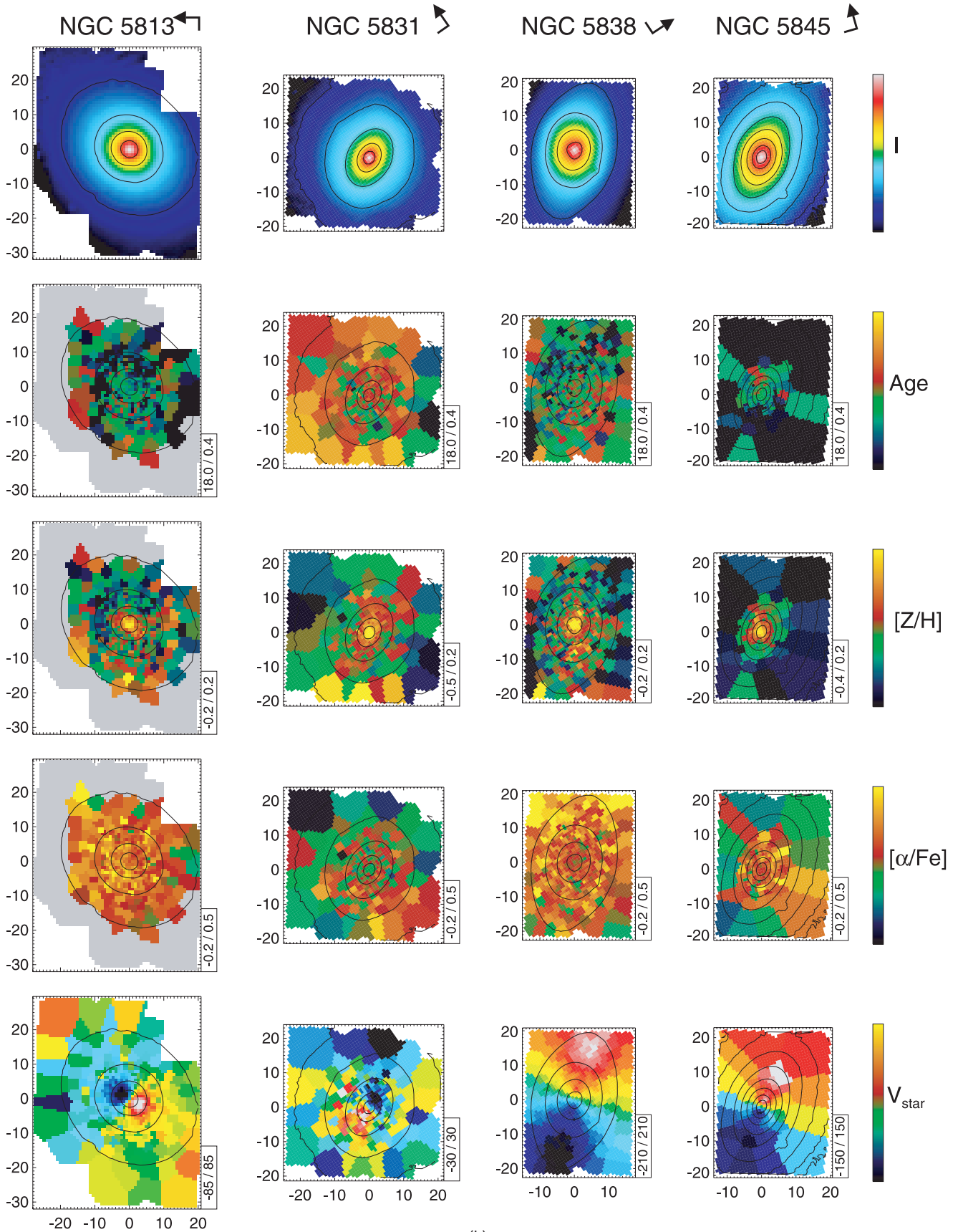


Figure 7 – continued.



(k)

Figure 7 – continued

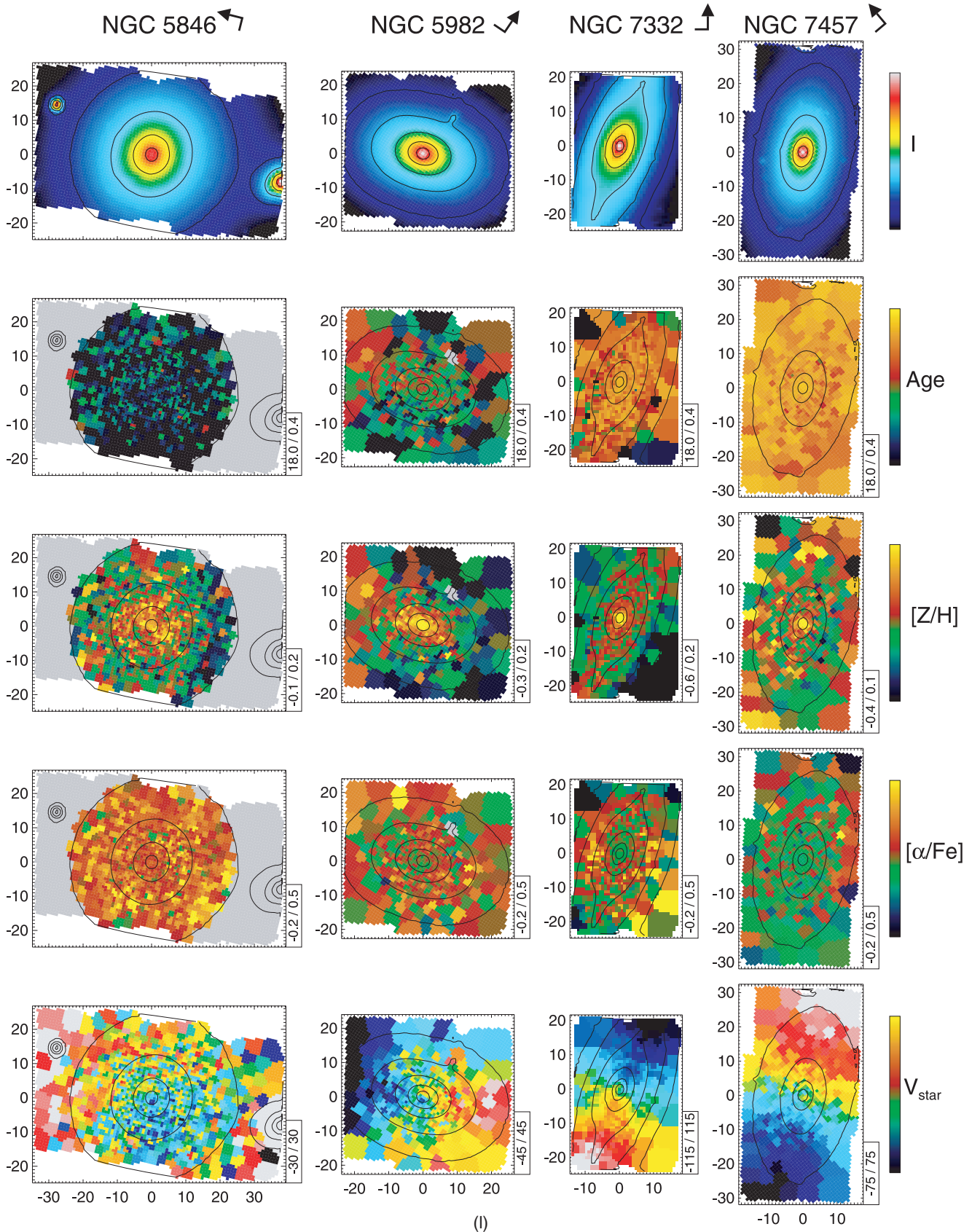


Figure 7 – continued

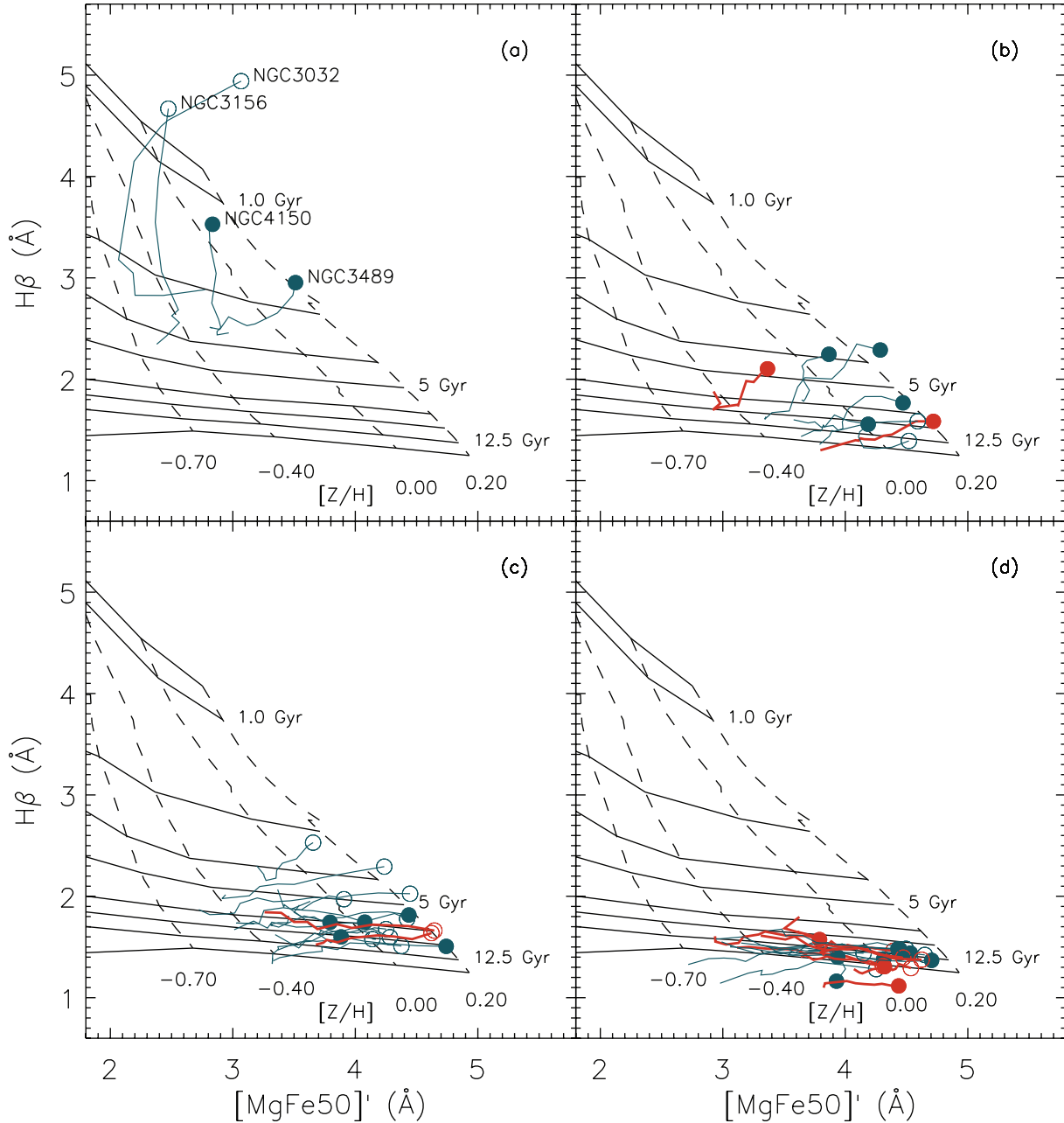


Figure 8. Age/metallicity diagnostic diagrams for our sample of the early-type galaxies in the SAURON survey. For each galaxy, a radial gradient averaged along isophotes is shown. The centre of each galaxy is indicated by a filled circle and open circle for cluster and field galaxies, respectively. The colour indicates whether a galaxy belongs to the fast rotators (blue) or slow rotators (red). Overplotted are stellar population models by Schiavon (2007). (a) Galaxies with an extended, recent star formation episode; (b) galaxies with signs of a central, spatially constrained, region of younger stellar populations; (c) galaxies with milder but spatially extended signs of a younger stellar population and (d) galaxies consistent with overall old stellar populations.

In marked contrast, individual galaxies (NGC 3032, NGC 3156, NGC 3489, NGC 4150 and NGC 7457) show age maps indicating a spatially extended, recent star formation episode covering large parts of the observed FoV with SSP-equivalent ages of less than ~ 3 Gyr (see Fig. 8a). Our age maps show that the youngest stellar populations in these galaxies are found in the central parts, with typically steep age gradients. Furthermore, ionized gas, optical dust features or even regular discs are detected in this group of objects (see Papers V and XVI and Table 2).

All of the above galaxies are also detected in a systematic single-dish CO survey of the SAURON sample (Combes, Young &

Bureau 2007), further supporting the scenario of recent star formation. Recently, the SAURON observations have been extended with auxiliary data in the NUV with *GALEX* imaging (Paper XIII) and in the mid-IR with *Spitzer*/Infrared Array Camera (hereafter IRAC) imaging and *Spitzer*/Infrared Spectrograph spectroscopy (Paper XV). The $NUV - V$ colour may be used to trace young stars (age < 1 Gyr) although conservative limits have to be chosen to avoid confusion with the UV-upturn phenomenon (e.g. O’Connell 1999, Paper XIII). Similarly, the existence of young stars and even ongoing star formation is closely connected to the presence of polycyclic aromatic hydrocarbon (PAH) emission around $8 \mu\text{m}$ (Paper XV).

Table 2. Summary of star formation indicators in the SAURON survey.

Name	Age ($R_e/8$) (Gyr)	σ_e (km s^{-1})	Flatter Mg <i>b</i> contours	CO	NUV	Mid-IR PAH	Optical dust	Ionized gas	Rotator (fast/slow)
(1)	(2)	(3)	(4)	(5)	(6)	(7)	(8)	(9)	(10)
Strong, widespread (post) starburst (see Fig. 8a)									
NGC 3032	0.9	90	N	Y	Y	Y	Y	Y (sf)	F
NGC 3156	0.9	65	N	Y	–	Y	Y	Y	F
NGC 4150	1.2	77	N	Y	Y	Y	Y	Y	F
NGC 3489	1.8	98	N	Y	–	Y	Y	Y	F
Spatially constrained, central (post) starburst (see Fig. 8b)									
NGC 4459	3.5	168	N	Y	Y	Y	Y	Y (sf)	F
NGC 4382	3.7	196	Y	N	–	N	N	(Y)	F
NGC 4550	4.3	110	Y	Y	Y	Y	Y	Y	(S)
NGC 4526	6.4	222	N	Y	Y	Y	Y	Y (sf)	F
NGC 5838	9.3	240	Y	N	N	Y	Y	Y	F
NGC 4477	9.7	162	Y	Y	N	Y	Y	Y	F
NGC 4552	10.2	252	N	N	N	N	Y	(Y)	S
NGC 524	>12	235	N	Y	N	Y	Y	Y	F
Spatially extended signs of SSP-equivalent younger age (see Fig. 8c)									
NGC 7457	2.8	78	N	N	Y	N	N	(Y)	F
NGC 7332	2.8	125	Y	–	–	N	–	Y	F
NGC 2549	3.7	145	N	N	–	–	N	Y	F
NGC 2685	5.1	96	N	Y	–	Y	Y	Y	F
NGC 3384	6.1	145	N	N	–	N	N	Y	F
NGC 2699	6.4	124	N	N	N	N	N	N	F
NGC 3377	6.7	138	Y	N	–	N	(Y)	Y	F
NGC 4270	8.1	122	N	N	–	N	N	N	F
NGC 5831	8.1	151	Y	N	N	N	N	(Y)	S
NGC 2768	8.9	216	N	Y	N	N	Y	Y	F
NGC 2974	8.9	233	Y	N	Y	Y	Y	Y	F
NGC 5982	8.9	229	Y	–	N	N	N	(Y)	S
NGC 474	9.3	150	N	N	Y	N	N	Y	F
NGC 4387	10.2	98	N	N	N	N	N	N	F
NGC 4564	10.7	155	Y	N	N	N	N	N	F
NGC 5845	11.2	239	N	N	N	(Y)	Y	N	F
SSP-equivalent ages consistent with old stellar populations (see Fig. 8d)									
NGC 4546	10.7	194	Y	N	N	N	N	Y	F
NGC 4458	10.7	85	N	N	N	N	N	N	S
NGC 821	11.2	189	Y	N	N	N	N	N	F
NGC 1023	11.7	182	N	N	(Y)	N	N	Y	F
NGC 3608	11.7	178	Y	N	–	N	Y	(Y)	S
NGC 4473	11.7	192	Y	N	N	N	N	N	F
NGC 4570	11.7	173	Y	N	N	N	N	N	F
NGC 5813	11.7	230	N	N	N	N	Y	Y	S
NGC 2695	>12	188	N	N	N	N	N	N	F
NGC 3379	>12	201	N	N	–	N	Y	(Y)	F
NGC 3414	>12	205	N	N	–	N	N	Y	S
NGC 4262	>12	172	N	N	–	N	N	Y	F
NGC 4278	>12	231	Y	N	N	N	Y	Y	F
NGC 4374	>12	278	N	N	N	N	Y	Y	S
NGC 4486	>12	298	N	N	N	N	Y	Y	S
NGC 4621	>12	211	Y	N	N	N	N	(Y)	F
NGC 4660	>12	185	Y	N	–	N	N	N	F
NGC 5198	>12	179	N	N	N	–	N	(Y)	S
NGC 5308	>12	208	N	N	N	–	N	N	F
NGC 5846	>12	238	N	N	N	N	Y	Y	S

Notes: This table provides a summary of the star formation indicators used in the SAURON survey. We group galaxies in four major categories and sort them by increasing SSP-equivalent age in each category. Column 1 lists the galaxy names. Column 2 gives the SSP-equivalent age over a circular aperture with radius $R_e/8$ (see also Table 1). Column 3 gives the average velocity dispersion over an aperture of R_e . Column 4 provides information on the shape of the Mg *b* contours compared to the isophotes (see Paper VI). Columns 5, 6 and 7 indicate detections for molecular gas (CO), NUV star formation signatures and mid-IR star formation detections from the studies of Combes et al. (2007), Paper XIII and Paper XV, respectively. The presence of optical dust and ionized gas emission is indicated in Columns 8 and 9 (see Papers V and XVI). Detections given in brackets ['(Y)'] are marginal, while 'Y (sf)' indicates signs of ongoing star formation as detected by the analysis of the gas emission in Paper XVI. Column 10 gives our classification into slow and fast rotators (see Paper IX for details). Since NGC 4550 features two counter-rotating discs it shows little overall rotation and hence is classified as slow rotator.

Remarkably, but perhaps not surprisingly, the four galaxies with the youngest SSP-equivalent ages in our sample (age <2 Gyr within an aperture of $R_c/8$) clearly exhibit signs of recent star formation in the NUV and in the mid-IR where data are available (see Table 2). This suggests residual ongoing star formation in this group of galaxies. Evidence for ongoing star formation is found in NGC 3032 even in our own emission-line analysis of the ionized gas (i.e. a very low [O III]/H β ratio) as demonstrated in Paper XVI.

The next youngest galaxy in our sample NGC 7457 with a central SSP-equivalent age of 2.8 Gyr ($R_c/8$) is only marginally detected in the UV and not detected in CO or by PAH emission in the mid-IR. We interpret the slightly older SSP-equivalent age and the absence of PAH emission in the mid-IR as evidence for an evolved version of the younger galaxies discussed above. It is interesting to note that all of the above mentioned galaxies have velocity dispersions of $\sigma_e \leq 100 \text{ km s}^{-1}$ ($M_{\text{dyn}} \leq 1.6 \times 10^{10} M_\odot$) and thus belong to the low-mass end of our sample. Paper XV argues that these kinds of galaxies are the product of recent gas-rich (minor) mergers where the cessation of star formation occurs in an ‘outside-in’ manner as the molecular gas is heated or consumed. The roughly equal distribution of co- and counter-rotating kinematic structures in these systems supports the external origin of the gas (Paper XV).

Another group of galaxies exhibit a more localized central region of young stars embedded within an otherwise older stellar system (see maps and Fig. 8b; NGC 4459, NGC 4382, NGC 4526, NGC 4550, NGC 4552, NGC 4477, NGC 5838 and NGC 524). In all but two cases (NGC 4382, NGC 4552), the recent star formation event – with sometimes residual ongoing star formation seen in the NUV, the mid-IR and the SAURON gas emission analysis (see Table 2) – is located in a thin, embedded disc clearly visible in the emission-line maps and the unsharp-masked optical dust images of Paper V. These thin stellar discs are typically co-rotating with the main body of the galaxy, albeit at the distinctly higher rotational speeds of discs. The metallicity maps (see also Section 4.1.2) of these galaxies show a spatially coincident region of enhanced metallicity, indicating the signs of ongoing metal enrichment due to disc star formation. NGC 524 is perhaps the least obvious member of this group of galaxies. It shows only very mild signs of younger stars in the centre,⁷ but it features a prominent face-on optical dust disc with a clear spiral pattern (see Paper V). If there are young stars associated with this thin disc, the near face-on orientation may dilute their contribution to the integrated line-of-sight. CO is detected in four out of six cases, with recent interferometric CO observations of NGC 4459, NGC 4526, NGC 4550 revealing molecular gas discs co-rotating with the stellar discs seen in the SAURON observations (Young, Bureau & Cappellari 2008; Crocker et al. 2009). Also, the *Spitzer* IRAC observations (Paper XV) clearly support the scenario of star formation in well-defined thin discs for this group of galaxies with detections for the majority of observed galaxies (see Table 2).

The SSP-equivalent ages derived for the regions affected by star-forming discs in the galaxies above mentioned range from about 3 Gyr to ages barely below the age of the Universe. This, of course, is a reflection of the luminosity weighting and involved mass fractions. Typically, these discs represent only a minor mass fraction of the total galaxy mass (e.g. Crocker et al. 2009), but contain contributions of very young (~100–300 Myr) stars (see also Kaviraj et al. 2009).

⁷ The S/N per observed spatial element was particularly low for this galaxy, and for radii larger than 20 arcsec with large bins the line strength indices are of modest quality.

We note that these thin, embedded discs with recent star formation typically reside in galaxies of intermediate-mass range with $\sigma_e = 160\text{--}240 \text{ km s}^{-1}$ ($M_{\text{dyn}} = 1\text{--}25 \times 10^{10} M_\odot$; see also Paper XV).

For the galaxies with circumnuclear star-forming discs or rings, Paper XV suggests a scenario where they experience a transient period of renewed star formation on top of an underlying much older population. The origin of the gas may be internal but also very minor mergers are conceivable. This process is a good candidate for producing the central, rapidly rotating and metal-rich stellar discs seen in many of our fast rotating galaxies (see Paper XII and Section 4.1.2).

There are two galaxies with a localized region of young stars (NGC 4382 and NGC 4552) lacking a detection of young stars in the NUV and the mid-IR. However, optical *Hubble Space Telescope* (*HST*) photometry and ground-based imaging provide evidence for a recent merger in the case of NGC 4382 (Lauer et al. 2005). In NGC 4382, the unusual bow-tie like distribution of the young stars also seen in an enhanced region of the metallicity map can be matched to the stellar kinematics, which show a marked twist in these areas with a strong depression in the velocity dispersion map (see Fig. 7f and Paper III), together with a central counter-rotating component as seen in the higher spatial resolution data of Paper VIII. We interpret this as a kinematically distinct stellar component (see also Paper XII) made of stars from a recent, but more than ~1 Gyr ago star formation episode. The ratio of mass involved in this star formation event to the total mass of the galaxy may be significantly higher compared to the mass ratio of the young stars in the embedded, thin discs seen in the other galaxies of this group.

For NGC 4552, the observed, mild increase in H β absorption strengths and thus inferred decrease in SSP-equivalent age of the central region are not supported by any of the other recent star formation indicators probed by our survey (see Table 2). Although this galaxy is known to exhibit a significant UV upturn (Bureau et al. in preparation), it is unlikely that the H β increase originates from this since none of the other slow rotator galaxies that show a UV-upturn (NGC 4374, 4486, 5198, 5846, 5982; Bureau et al. in preparation) exhibits a clear central increase in H β absorption strength (see Paper VI) or corresponding decrease in SSP-equivalent age. Due to the significant amount of gas emission present in the centre of this galaxy (see Papers V and XVI), it is also possible that the H β absorption has been somewhat overcorrected.

Typically, star formation and the resulting younger SSP-equivalent ages are found towards the centre of early-type galaxies and star formation takes place in a thin disc/ring morphology (see Figs 8a–c and also Paper XV). However, there is also evidence for star formation outside the nuclear regions in two galaxies. (1) NGC 474 shows an age map with a relatively old central part (~9 Gyr) while the SSP-equivalent age becomes younger towards larger radii ($r \geq 6$ arcsec). This observation is supported by blue NUV-optical colours at the same radii (see Paper XIII) and is perhaps connected to the famous shell structures of NGC 474 (Turnbull, Bridges & Carter 1999). (2) NGC 2974 shows significant star formation in a ring-like structure, both clearly exhibiting signs of recent star formation in the NUV and in the mid-IR, outside the observed FoV of the SAURON observations (Jeong et al. 2007, Paper XV). There is also H I detected in a ring-like configuration (Weijmans et al. 2008). We detect only mild signs of younger stellar populations.

Besides the galaxies with strong signs of recent star formation or spatially constrained star formation connected to thin, embedded discs, there is a sizable group of galaxies (~30 per cent of the

sample) that show intermediate SSP-equivalent ages (3–11 Gyr) over large parts of the observed FoV (in increasing order of central $R_e/8$ SSP-equivalent age: NGC 7457, NGC 7332, NGC 2549, NGC 2685, NGC 3384, NGC 2699, NGC 3377, NGC 4270, NGC 5831, NGC 2768, NGC 5982, NGC 4387, NGC 4564, NGC 5845). With only two exceptions [the polar ring galaxy NGC 2768 (Crocker et al. 2008) and NGC 2685] these galaxies are not detected in CO, indicating that they have exhausted their molecular gas supply and are now evolving passively. Moreover, neither the dust maps nor the NUV or mid-IR indicators show evidence for recent (<1 Gyr) star formation. This is consistent with a star formation episode in these galaxies which is long enough ago to be devoid of dust and very young stars, but recent and massive enough to be traced by the $H\beta$ index and thus our SSP-equivalent age maps. For these galaxies (see also Fig. 8c) we find typically flat age maps or only mildly increasing SSP-equivalent age as a function of radius.

Last, but not the least, we have the group of galaxies that show line strength indices consistent with overall old stellar populations, at least within the sensitivity of our line strength observations and stellar population analysis (Fig. 8d). Eight out of these 20 galaxies are classified as slow rotators in Paper IX and it is indeed the group of galaxies with old stellar populations where we find most of the slow rotators (see also Section 4.3). Two galaxies (NGC 2695 for larger radii and NGC 4486 for all radii) show $H\beta$ line strength which is below the stellar population model predictions and therefore lead to non-physically large SSP-equivalent ages. A thorough check of the data-reduction procedure revealed nothing special for these galaxies and thus we can offer no explanation to why the $H\beta$ line strength is so weak for these two galaxies.

We note that, when explored at higher spatial resolution, individual galaxies in the ‘old’ group can show signs of recent star formation. For example, *HST* imaging of NGC 4570 (van den Bosch & Emsellem 1998) reveals evidence for a bar-driven ring of young stars (~ 2 Gyr) at a radius of 1.7 arcsec at the presumed location of a bar inner Lindblad resonance (ILR).

It is interesting to explore the stellar populations of the class of early-type galaxies with KDCs. We define them here as sub-components that either rotate around a different axis to the main galaxy or rotate around the same axis, but with an opposite sense of rotation and thus are distinct from the young discs discussed above. In Papers III, VIII and XII, 13 galaxies of the SAURON survey were identified to harbour KDCs. Broadly speaking there appear to be two types of KDCs: kiloparsec-scale structures which are found almost exclusively in slow rotating galaxies with predominantly old stellar populations (NGC 3414, NGC 3608, NGC 4458, NGC 5198, NGC 5813, NGC 5831, NGC 5982), and more compact KDCs showing a range in SSP-equivalent ages with a preference towards more recent star formation episodes (NGC 3032, NGC 4150, NGC 4382, NGC 4621, NGC 7332, NGC 7457; see Paper VIII). While the central, thin discs discussed above show a prominent connection between young stars, optical dust, nebular emission, NUV and mid-IR star formation indicators and enhanced metallicity, it is remarkable that most of the large-scale KDCs do not show an equivalent, significant signature in the stellar population maps. NGC 5831 and NGC 5982 do exhibit mild signs of a contribution from young stars, but the spatial location of the KDCs and that of the young stars is not well correlated. Additionally, the metallicity maps (see Section 4.1.2) also do not show a significant correlation with the rotation direction of the KDC, but rather follow a normal, smooth radial behaviour. In summary, any assembly and star formation scenario designed to explain the observed

large-scale KDCs must account for the absence of significant stellar population parameter signatures (i.e. age, metallicity or abundance ratio).

This can be achieved, for example, if the formation process was completed a long time ago (e.g. Davies et al. 2001). However, other possibilities are being explored too. A recent dynamical study (van den Bosch et al. 2008) applying triaxial orbit-based models to the prominent KDC galaxy NGC 4365 (see also Bender 1988; Davies et al. 2001) shows that the observed KDC is not physically distinct from the main body, but rather caused by a superposition of orbits. A more systematic study of the dynamics of KDC galaxies is in preparation (van den Bosch et al.) but it may well be that a significant fraction of the observed large-scale KDCs are not dynamically distinct subcomponents, but rather are the result of a projection of orbits from a more extended structure, thus naturally explaining the absence of any distinct stellar population signatures.

4.1.2 Metallicity and abundance ratio maps

For galaxies with old stellar populations, the abundance ratio maps often show to the first order no or only mild positive radial gradients with values of $[\alpha/\text{Fe}] \simeq 0.2\text{--}0.4$ (red to yellow colour shading). The most significant structures, over and above the generally rather noisy appearance of the maps, are typically connected to the presence of (very) young stellar populations, which lead to lower, more solar values of $[\alpha/\text{Fe}]$ (see e.g. NGC 3156, NGC 4150 and NGC 7457). The metallicity maps generally show negative gradients with increasing radius, often roughly consistent with the morphology of the light profiles and consistent with many of the earlier long slit studies (e.g. Carollo, Danziger & Buson 1993; Davies et al. 1993; Sánchez-Blázquez et al. 2007). Two remarkable outliers from this trend exist. NGC 3032 and NGC 4150, showing a central peak in metallicity with a surrounding ring of depressed metallicity. These two galaxies are among the most extreme examples of a recent starburst in our sample (see Table 2). Due to the degeneracies between star formation age and young star mass fractions, as well as the biases described in Section 3.3, the stellar population maps of these galaxies are difficult to interpret and a simple interpretation may be misleading.

Mean metallicity and $[\alpha/\text{Fe}]$ gradients averaged along isophotes are described in more detail in Section 4.2 while we concentrate in this Section on the two-dimensional aspects of the maps.

In Paper VI, we found that the $\text{Mg } b$ isoindex contours appear to be flatter than the isophotes of the surface brightness for about 40 per cent of our galaxies without significant dust features (also see Table 2). This flattening is almost always associated with significant rotation in the galaxies (see also Paper XII) and we inferred from this that the fast-rotating component features a higher metallicity and/or an increased $[\alpha/\text{Fe}]$ ratio compared to the galaxy as a whole. With the stellar population maps presented in this study we confirm that the metallicity is enhanced for fast rotating systems such that the iso-metallicity contours appear more flattened than the isophotes (prominent examples include NGC 4564, NGC 4473, NGC 4621 and NGC 4660; see Fig. 9). However, the region of enhanced metallicity is typically connected with a mild *decrease* in our abundance ratio maps (see also Fig. 9).

For individual galaxies such as NGC 2549 and NGC 3377 the region of increased metallicity is connected to the presence of younger stellar populations in a rotating structure with disc-like kinematics. For other galaxies there is only mild (e.g. NGC 4564) or no (e.g. NGC 4660) evidence for younger populations. It is

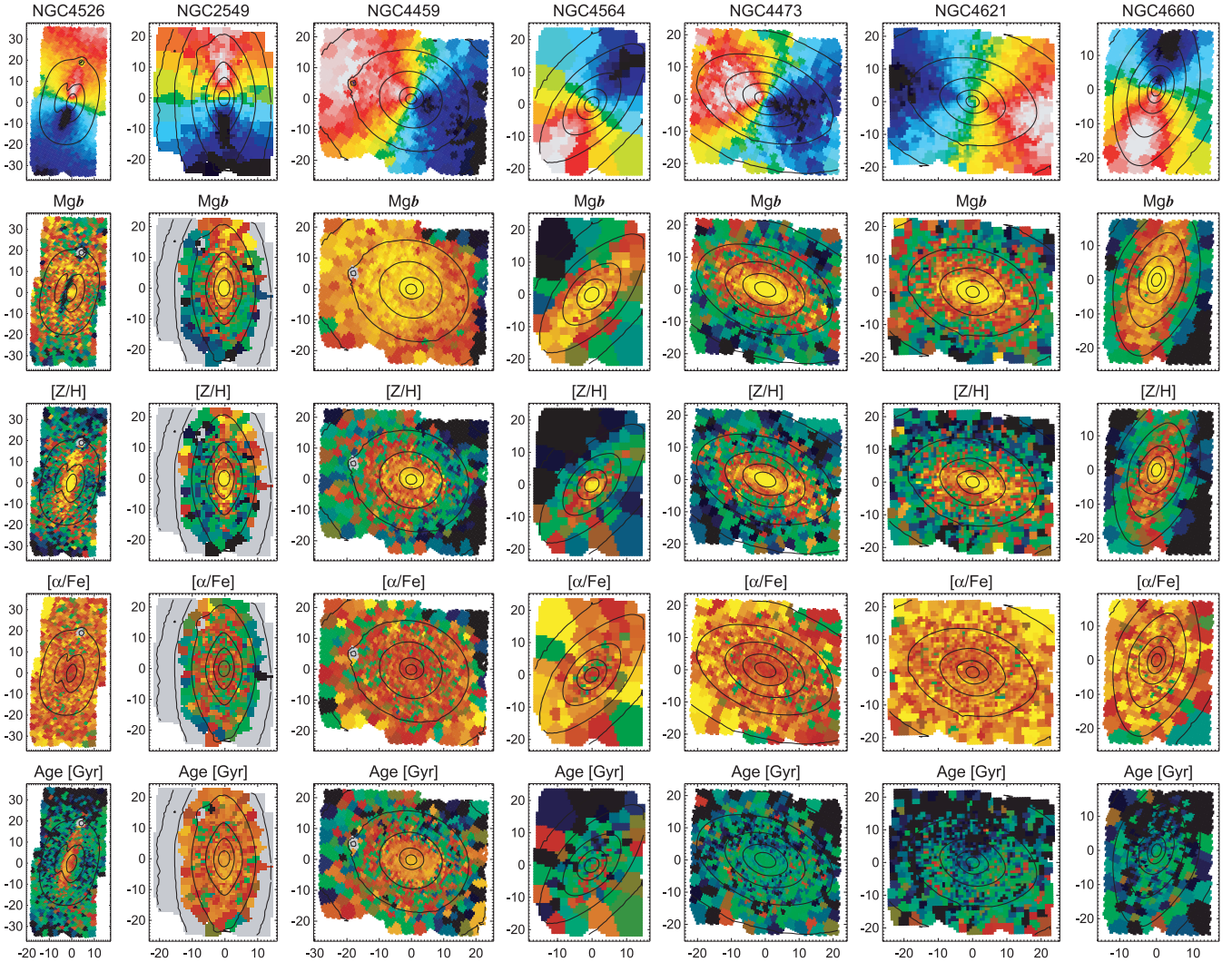


Figure 9. Prominent examples of fast rotators with a distinct, central disc-like component. For each galaxy we show from the top, the stellar velocity field, the Mgb line strength map (see Paper VI), the metallicity map, the abundance ratio map $[\alpha/Fe]$ and the SSP-equivalent age map. The disc-like components can be clearly seen in the velocity fields and are reflected in enhanced Mgb and $[Z/H]$ regions and mild depressions in the $[\alpha/Fe]$ maps. NGC 4526 and NGC 4459 are examples of currently ongoing residual star formation in a disc. Bins shown in grey colour for NGC 2549 indicate regions of low S/N ratio and thus doubtful line strength measurements. Note the varying spatial scales shown for different galaxies; units are given in arcsec.

tempting to associate these flattened regions of enhanced metallicity and somewhat lower abundance ratios with the more recent star formation seen in thin discs in galaxies such as NGC 4459 and NGC 4526 (see Fig. 9). Taken together, a scenario emerges in which the star formation event that created the fast rotating disc-like structure is distinct from the formation of the galaxy main body, which took place at a later stage and on somewhat longer time-scales, leading to an increased metallicity and reduced abundance ratio value.

Norris, Sharples & Kuntschner (2006) demonstrated in their detailed study of the lenticular galaxy NGC 3115 that a simple spheroid + disc formation model, where the old spheroid has $[\alpha/Fe] = 0.3$ and the somewhat younger disc shows close to solar abundance ratios, works well to explain the observed stellar population trends in this galaxy.

In the SAURON sample, we find good evidence for this secondary star formation in disc-like structures for low- to intermediate-mass ($\sigma_e = 100\text{--}160 \text{ km s}^{-1}$), fast-rotator galaxies such as NGC 3377 and NGC 4550 where the young stars are still prominently seen in the

SSP-equivalent age maps affecting large regions of the galaxy. Can we also find evidence of this type of secondary star formation in older galaxies?

For more massive galaxies ($\sigma_e > 160 \text{ km s}^{-1}$) the disc formation and increased metallicity are typically constrained to a central location involving only a minor fraction of the total mass of the galaxy (e.g. NGC 4459, NGC 4526; Fig. 9). However, examining the $[\alpha/Fe]$ maps more carefully, one can see central depressions in about 25 per cent of the galaxies (e.g. NGC 821, NGC 1023, NGC 2699, NGC 4270, NGC 4387, NGC 4473, NGC 4546, NGC 4564, NGC 4570, NGC 4621, NGC 4660, NGC 5838). All of these galaxies are classified as fast rotators and exhibit overall old ($>9 \text{ Gyr}$) stellar populations, while the depression in $[\alpha/Fe]$ is highly correlated with an enhancement of the metallicity estimates in the same spatial position. A careful examination of the age maps often also reveals a weak signature of a contribution from a younger stellar population in these central regions as compared to the outer regions. However, the most important connection to mention is that all of the galaxies with central depressions in $[\alpha/Fe]$ show pinched

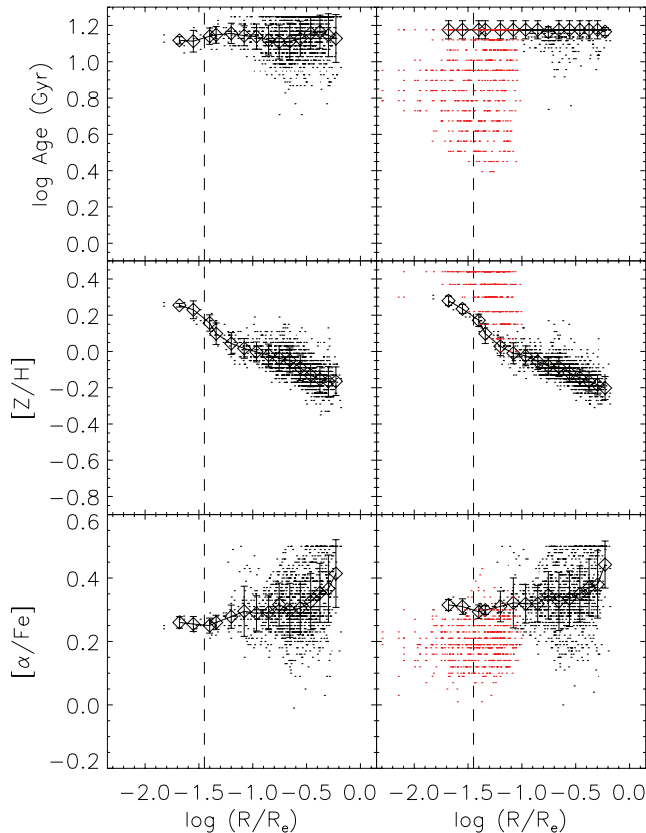


Figure 10. Radial gradients of stellar population estimates for the fast rotator galaxy NGC 4621. The black dots represent individual bins while the solid line connects values averaged along isophotes where radial bins are indicated by open diamonds. The stellar population estimates are shown as derived from Schiavon (2007, left-hand column) and TMB03 (right-hand column) models. The red dots show the results from high spatial resolution OASIS observations (see Paper VIII) where the stellar population estimates were derived with TMB03 models, however, using a larger set of Lick/IDS indices, namely $H\beta$, Fe5015, $Mg\ b$, Fe5270, Fe5335 and Fe5406. The vertical dashed lines indicate a radius of 2 arcsec.

iso-velocity contours towards the centre indicating the existence of a central fast-rotating, disc-like component.⁸ Remarkably, all galaxies of the above group that are included in the analysis of *HST* imaging by Lauer et al. (2005, 6/12 galaxies) reveal the signature of a stellar disc in the central regions. Figs 10 and 11 show radially averaged stellar population gradients for selected galaxies where the central depressions in $[\alpha/Fe]$ are more apparent.

The kinematics analysis of our velocity maps presented in Paper XII suggested that all fast rotators contain flattened, fast-rotating components contributing at various levels to the total light of the galaxy. For example, there are disc-dominated galaxies such as NGC 3156 and NGC 2685 and more bulge-dominated systems such as NGC 821 and NGC 4660 (see Paper XII), the latter showing largely old stellar populations. Furthermore, 70 per cent of the sample shows evidence for distinct, multiple kinematic components.

A picture emerges where essentially all fast rotator galaxies have seen a period (often multiple periods) of secondary star formation

in kinematically disc-like components on top of an older, spheroidal component. This picture is perhaps well known and accepted for classical S0s with small bulge to disc ratios (e.g. Fisher, Franx & Illingworth 1996; Norris et al. 2006). However, we find sub-components with disc-like kinematics and distinct stellar populations in all fast rotators ranging from galaxies classified as Sa to (elongated) ellipticals: (a) central very young, still star-forming discs in e.g. NGC 4526 (Sa), NGC 4459 (S0; Papers XIII and XV), (b) intermediate-age systems devoid of any ongoing star formation but clear detections of a younger, metal rich and $[\alpha/Fe]$ depressed component with disc-like kinematics as seen in NGC 2699 (E) and NGC 3384 (SB); and (c) in the systems with largely old stellar populations where the star formation event connected to the disc-like kinematics is mostly evidenced by a raised metallicity in combination with lower $[\alpha/Fe]$ ratios as seen in e.g. NGC 4621 (E5) and NGC 4660 (E5). Fig. 9 presents an overview of selected fast rotators with metal-rich, but $[\alpha/Fe]$ -depressed disc-like components ranging from still star-forming discs as found in NGC 4526 to overall old stellar populations as seen perhaps in NGC 4660.

The frequent disc-like structures observed at various scales in our sample of fast-rotating early-type galaxies suggest dissipative processes play a major role in their formation. The very central stellar discs seen in *HST* imaging and the somewhat larger disc-like kinematic structures with increased metallicity and depressed $[\alpha/Fe]$ seen in our observations of fast rotators match well with the recurring but transient circumnuclear star formation seen in the mid-IR *Spitzer* observations described in Paper XV. The rotational support on larger scales for *low-mass* galaxies, which are also often showing signs of younger stellar populations, is probably connected to gas-rich (major) mergers adding a widespread, fast-rotating younger component to the galaxies (see also Hoffman et al. 2009). It is not obvious that all fast-rotating components on larger scales in early-type galaxies can be produced in this way. However, recent integral field unit observations for $z = 2-3$ galaxies revealed striking evidence for a transient phase of clumpy, turbulent disc formation fed by rapid cold flows (Genzel et al. 2008). The old, *large-scale* disc-like structures seen in our sample of galaxies could well be the fossil relic of such a cold flow mode of star formation seen at higher redshift. The rotational support and the relatively short time-scale (≤ 1 Gyr) of the secular evolution in these ancient turbulent gas-rich discs seem consistent with our observations (see also Elmegreen, Bournaud & Elmegreen 2008).

The slow rotators in our sample (excluding NGC 4550 with its two counter-rotating discs) mostly show flat $[\alpha/Fe]$ maps with metallicity gradients consistent with the isophotes. This supports their likely different formation path as already argued in Papers IX, X and XII. There are, however, four slow rotators which show abundance ratio maps indicating a somewhat depressed $[\alpha/Fe]$ ratio towards the centre: NGC 4552, NGC 5198, NGC 5831 and NGC 5982. This group of galaxies, which partially also shows weak signs of a contribution from a younger stellar population, may indicate that the class of slow rotators is perhaps not as homogeneous in their stellar populations as their kinematics may suggest.

A few words of caution with regard to the results presented so far are due. We note that as shown in Paper VI, the $Mg\ b$ index is a very good *observational* tracer of the increased metallicity of the disc-like structures. However, in the presence of young stellar populations (SSP-equivalent age ≤ 3 Gyr) the $Mg\ b$ index reacts significantly to age and this causes a decrease in absorption strength compared to an old population with the same metallicity. For example, NGC 4382 (see Paper VI) shows a central $Mg\ b$ -index depression which renders the $Mg\ b$ index a less useful tool to detect

⁸ We note that due to inclination effects, edge-on discs in the centre are more visible than face-on examples.

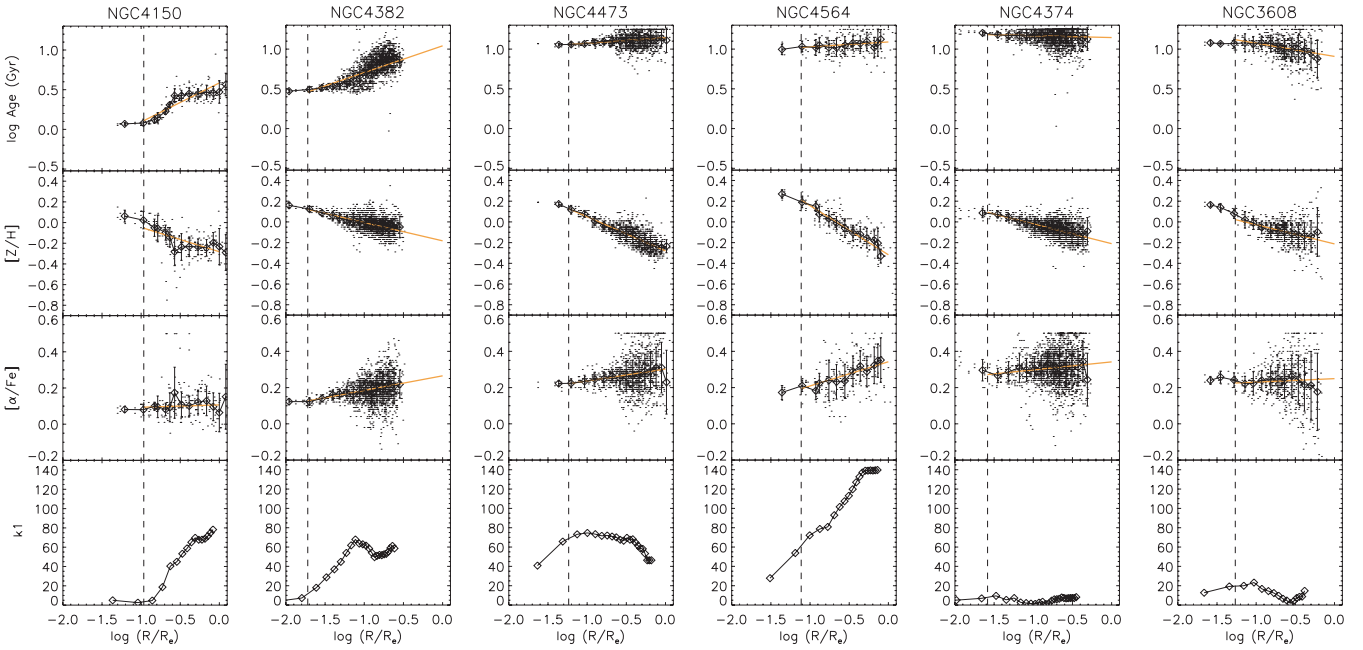


Figure 11. Examples of radial profiles, averaged along isophotes, of SSP-equivalent age, metallicity and $[\alpha/\text{Fe}]$ estimates (open diamonds). We fit an error-weighted straight line (orange solid line) to each profile for all data available between 2 arcsec (vertical dashed lines) and R_e . See text for details. Small black points represent individual bins in the stellar population maps. The bottom panels show the $k1$ parameter – a measure of the maximum rotation velocity – from the kinemetry analysis of Paper XII.

metallicity enhancements connected to disc-like kinematics in these kind of galaxies.

Using the Thomas et al. models instead of the Schiavon models does not alter our main findings and conclusions discussed above. In fact, the signs of distinct stellar populations in the regions of disc-like kinematics would be more pronounced in metallicity for galaxies with old stellar populations. In Fig. 10, we show results for radially averaged stellar population estimates derived from both stellar population models for NGC 4621 (for details of the procedure see Section 4.2).

The main limitation of our abundance ratio estimates is the limited number of indices available for the analysis. New observations covering large regions of the galaxies as well as a longer wavelength range, thus including more indices, are needed to confirm the above findings.

4.2 Average stellar population gradients

Average stellar population gradients can be used to study the formation history of early-type galaxies since different formation models predict different gradients. In a nutshell, monolithic collapse models (Carlberg 1984; Arimoto & Yoshii 1987; Pipino, D’Ercole & Matteucci 2008) predict steep metallicity gradients (ranging from $\delta[Z/H]/\delta\log R = \Delta[Z/H] = -0.35$ to -1.0) with metal-rich centres whereas hierarchical models, following a merger tree, predict shallower gradients due to the dilution of any line strength gradients existing in the pre-merger units (White 1980; Kobayashi 2004). However, adding secondary star formation, introduced by gas-rich mergers with a range in degree of dissipation, will typically lead to enhanced metallicity over the inner regions and thus again steeper metallicity gradients. The metallicity gradients are predicted to be strongly correlated with the efficiency of the dissipative process, and to only weakly depend on the remnant mass (Kobayashi 2004; Hopkins et al. 2009a,b).

In this section we derive robust and SSP gradients for SSP-equivalent age, metallicity and abundance ratio by averaging the measurements along lines of constant surface brightness (isophotes) with equal steps in \log flux. This approach does not take into account the deviations from e.g. metallicity or $[\alpha/\text{Fe}]$ contours with respect to isophotes, but does provide valuable estimates of *mean* gradients which can be investigated throughout the whole sample and compared to the predictions of simulations. Due to the two-dimensional coverage of our data these mean radial gradients can be determined with very good precision. The average value in each radial bin is derived after applying a 3σ clipping algorithm. The radius for each bin is calculated as the median major axis radius normalized to the effective radius (see Table A1) along the major axis $a_e = R_e/\sqrt{1-\epsilon}$, where R_e is the effective radius and ϵ is the average ellipticity of the galaxy within the SAURON field.

In Fig. 12, we show the radial profiles of SSP-equivalent age, metallicity and abundance ratio as function of $\log(R/R_e)$ as derived from the data. The following conclusions can be inferred from the diagram: (1) if the central parts of a galaxy show old (>9 Gyr) SSP-equivalent ages, then age gradients remain typically flat. (2) In contrast, the presence of young stellar populations in the centre typically leads to age gradients such that older SSP-equivalent ages are found at larger radii.⁹ This observation supports the scenario of potentially multiple, centrally located star formation events which add to the older, underlying stars. (3) Excluding galaxies with significant recent episodes of star formation (central age ≤ 3 Gyr), metallicity gradients appear remarkably homogeneous with a mean value of -0.28 dex per $\log(R/R_e)$ and an rms of 0.12. There is a significant range in central metallicity not obviously connected to the age of the stellar population. (4) Abundance ratio gradients are

⁹ A notable exception to this trend is NGC 474 which shows star formation at larger radii (see also Paper XIII and Section 4.1.1).

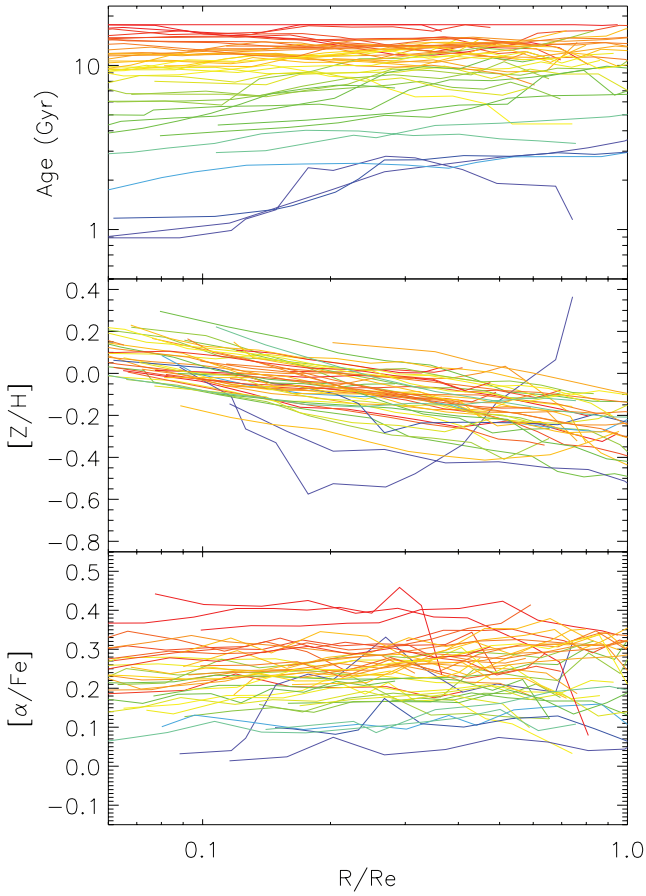


Figure 12. Overview of radial profiles, averaged along isophotes, of SSP-equivalent age, metallicity and $[\alpha/\text{Fe}]$ for the 48 early-type galaxies in the SAURON sample. The colour coding reflects central $R_e/8$ SSP-equivalent age with red referring to old stellar populations and blue to young ones (see top plot).

typically consistent with a flat distribution or are mildly positive gradient [median value of 0.06 dex per $\log(R/R_e)$]. Overall, there is a trend in the sense that the oldest galaxies have the strongest non-solar abundance ratios (see also Fig. 6).

For each galaxy we fit an error-weighted straight line to the stellar population values at a given radius such that age gradients are defined as

$$\Delta \log \text{Age} = \frac{\delta \log \text{Age}}{\delta \log(R/R_e)}, \quad (5)$$

where age is measured in Gyr. A similar definition is used for the measurements of the gradients in $[Z/H]$ and $[\alpha/\text{Fe}]$, denoted as $\Delta [Z/H]$ and $\Delta [\alpha/\text{Fe}]$, respectively. Examples of the fits are shown in Fig. 11 for galaxies representative of the group of fast rotators with young central discs (NGC 4150, NGC 4382), ‘old’ fast rotators with evidence for an embedded disc-like component (NGC 4473, NGC 4564) and galaxies from the group of slow rotators (NGC 4374, NGC 3608).

The error of the measurements in each surface brightness bin is taken as the 1σ scatter of the data-points within this bin after applying a 3σ clipping algorithm. We further restrict the fitting range to all available data with radii between 2 arcsec and R_e . The inner $r < 2$ arcsec regions are excluded from the fit in order to avoid biases due to seeing effects. The overall quality of the fits is good and also the assumption of linear gradients per $\Delta \log R$ is reasonable,

with the exception of some galaxies with contributions from very young stars (see e.g. NGC 4150 and NGC 4382 in Fig. 11).

In Figs 13 and 14, we explore the connection between stellar population gradients and central stellar population estimates within an aperture of $R_e/8$, as well as the connection between stellar population gradients and global kinematic parameters such as mean velocity dispersion within one effective radius σ_e , the dynamical mass M_{dyn} (see equation 3) and the degree of rotational support as measured by λ_R .

As was already apparent from Fig. 12, old (≥ 8 Gyr) galaxies generally do not show significant age gradients (mean gradient 0.02 ± 0.13 ; the error reflects the 1σ standard deviation of the gradients), whereas young, fast rotator galaxies typically show positive age gradients (corresponding to a younger centre; mean gradient 0.28 ± 0.16). Metallicity gradients are, with two exceptions (NGC 3032, NGC 524), all negative with a median value of -0.27 . The mean metallicity gradient for old (age ≥ 8 Gyr) galaxies is -0.25 ± 0.11 . There is, however, a trend with λ_R in the sense that fast rotators have on average the steeper metallicity gradients with a large scatter at high λ_R .

The relation between SAURON line strength index gradients and stellar population gradients with the local escape velocity V_{esc} was explored in Scott et al. (2009). A tight correlation between V_{esc} and the line strength indices is found. For Mg b , this correlation exists not only between different galaxies but remarkably also inside individual galaxies – it is both a local and global correlation. When index measurements are converted to stellar population estimates the galaxies are found to be confined to a good approximation to a plane in the four-dimensional parameter space of SSP-equivalent age, metallicity ($[Z/H]$), abundance ratio ($[\alpha/\text{Fe}]$) and V_{esc} . The observed tight connection between stellar populations and the gravitational potential, both locally and globally, presents a strong constraint on galaxy formation scenarios.

Spolaor et al. (2009) noticed a mass–metallicity gradient relation for early-type galaxies where low-mass galaxies ($\lesssim 3.5 \times 10^{10} M_\odot$) form a tight relation of increasing metallicity gradient with increasing mass. For galaxies above the transition mass there is a clear downturn in metallicity gradient with increased scatter. Our analysis is consistent with these observations (see Fig. 14, middle panel, but also see Rawle, Smith & Lucey 2010). The fraction of slow rotators increases with increasing mass and the most massive galaxies are slow rotators (see Paper IX). Furthermore, there is a weak trend among the slow rotators in the sense that the galaxies with the smallest λ_R exhibit the shallowest metallicity gradients. This trend clearly needs confirmation with a larger sample of slow rotators.

These observations suggest that the formation and subsequent evolution of low-mass early-type galaxies (which are dominated by fast rotators) lead to a connection between galaxy mass and metal enrichment such that the steepest metallicity gradients are achieved for masses of $\sim 3.5 \times 10^{10} M_\odot$. All these galaxies are rotationally supported and feature strong disc-components suggesting gas-rich mergers and accretion to play an important role. We emphasize that low-mass galaxies with young *and* old SSP-equivalent ages follow this relation and thus secondary star formation due to gas-rich (minor) mergers (see Section 4.1.1; Paper XV) does not destroy the trend. For more massive galaxies (above $\sim 3.5 \times 10^{10} M_\odot$) the relative influence of the various star formation and assembly processes which determine the galaxies’ properties seem to change. We observe a large scatter of metallicity gradients with an overall downturn with mass and increased fraction of slow rotators towards the most massive systems ($> 10^{11} M_\odot$). The observed scatter may

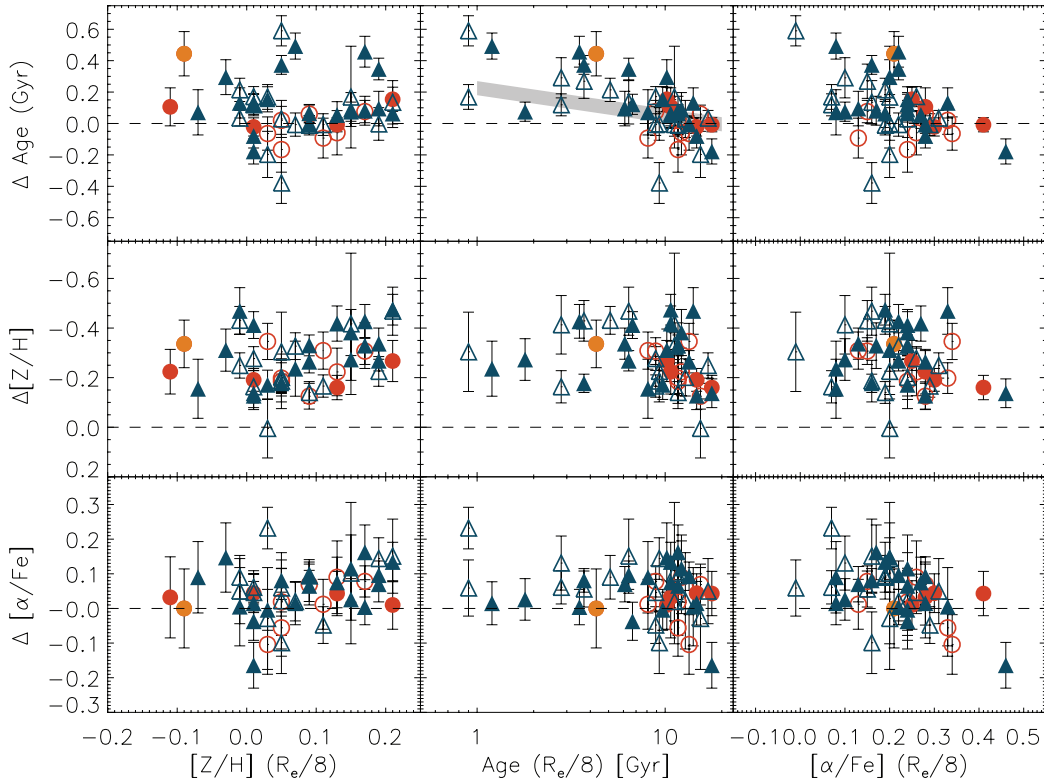


Figure 13. Age gradient, metallicity gradient and $[\alpha/\text{Fe}]$ gradient *versus* metallicity, age and $[\alpha/\text{Fe}]$ measured within a circular aperture of $R_e/8$. Fast and slow rotators are indicated by blue triangles and red circles, respectively. NGC 4550, classified as slow rotator due to two counter-rotating discs, is shown as orange filled symbol. Cluster and field galaxies are shown as filled and open symbols. In the top middle panel, we show in grey the region occupied by the simulations of Hopkins et al. (2009a, their fig. 29).

be the result of competing processes such as minor gas-rich mergers building disc-like structures over extended regions with rather shallow metallicity gradients, circumnuclear star formation in rings and discs leading to steeper metallicity gradients, particularly in the centre, and gas-poor (major) merging removing the signature of ordered motion and also weakening metallicity gradients in the most massive remnants. Consistent with this picture, we find the most massive systems to be slow rotators that exhibit relatively shallow metallicity gradients and are devoid of any signs of recent star formation (see also Paper XV). Brightest cluster galaxies, which are underrepresented in our sample, may deviate from the trend (e.g. Brough et al. 2007; Spolaor et al. 2009). However, the analysis of the projected axial ratio distribution of quiescent galaxies in the Sloan Digital Sky Survey (van der Wel et al. 2009) demonstrates that galaxies above a mass of $\sim 10^{11} M_\odot$ have essentially a spheroidal shape without major disc contribution whereas the lower mass systems show a large range in axial ratios.

The average $[\alpha/\text{Fe}]$ gradients are consistent with zero for the slow rotators while a significant fraction of the low-mass, fast rotators show mildly *positive* gradients which we interpret as signs of the contributions from the central, more metal-rich and abundance-ratio depressed regions with disc-like kinematics. The mean $[\alpha/\text{Fe}]$ gradients of the fast and slow rotators are 0.060 ± 0.012 and 0.023 ± 0.016 , respectively (the mean was determined with an outlier resistant bi-weight method and the errors reflect errors on the mean values).

In the recent simulations of major mergers of gas-rich discs by Hopkins et al. (2009a), a large range of metallicity gradients is found. They emphasize the importance of the degree of dissipation

in the central, merger-induced starburst for the resulting metallicity gradient. Their predictions (shown as grey shaded regions in Figs 13 and 14) broadly agree with our observations. This includes the overall downturn in metallicity gradient with increasing mass. For galaxies in common we specifically explore the correlation between our observed metallicity gradients with their observed measurements of extra light f_{extra} and compare this also with their predictions from simulations (grey shaded area) in Fig. 15. While the predictions broadly agree with the observations, a firm conclusion is not possible with this limited number of galaxies.

4.3 Scaling relations of integrated stellar population estimates

After the presentation of the stellar population maps (Section 4.1) and the average gradients (Section 4.2), we now discuss more global SSP-equivalent stellar population parameters. Our integrated measurements were derived by averaging the (luminosity-weighted) spectra within a circular aperture with a radius of one R_e and re-measuring the line strength indices. Small aperture corrections, as described in Paper VI, had to be applied for 28 galaxies. From the resulting line strength values (Table A1), we derived the stellar population estimates as described in Section 3.2 and presented in Table 1. We emphasize that these ‘global’ estimates of SSP-equivalent stellar population parameters derived from data covering essentially one effective radius (half the light) for nearby galaxies are much more representative of the galaxies as a whole compared to the typically central (often $R_e/8$) values used in the past (e.g. Kuntschner 2000; Trager et al. 2000; Thomas et al. 2005).

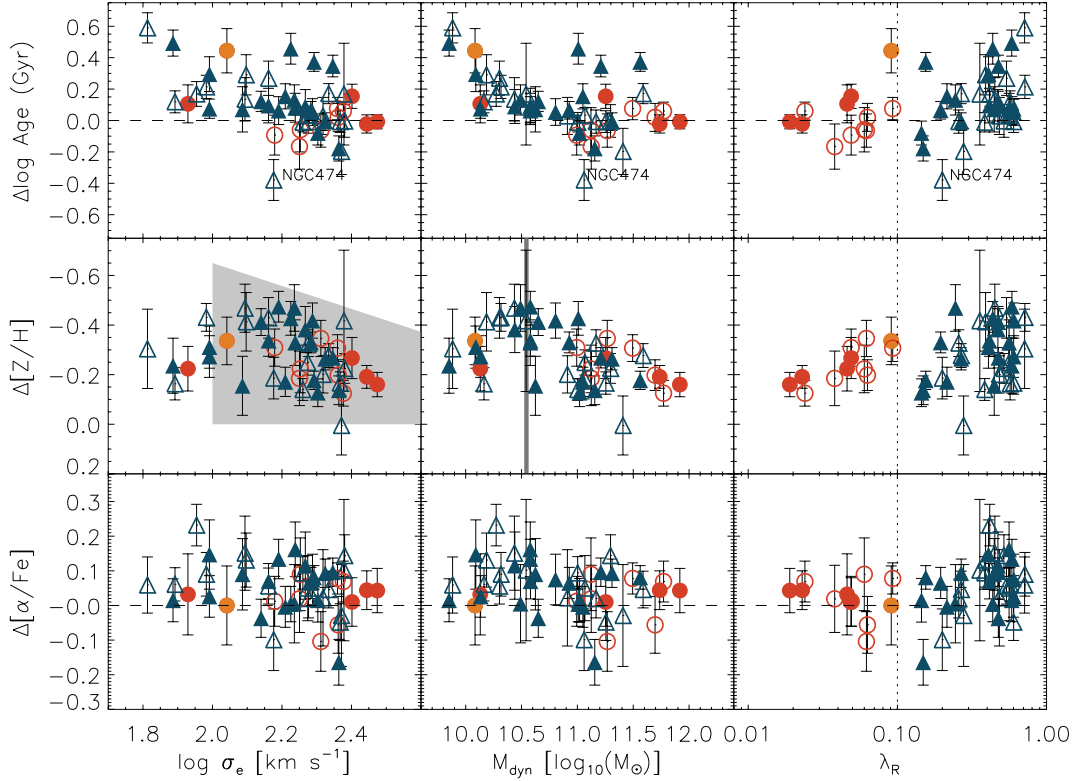


Figure 14. Age gradient, metallicity gradient and $[\alpha/\text{Fe}]$ gradient versus $\log \sigma_e$, dynamical mass M_{dyn} and $\log \lambda_R$ for the 48 early-type galaxies in the SAURON sample. Fast and slow rotators are indicated by blue triangles and red circles, respectively. Cluster and field galaxies are shown as filled and open symbols. NGC 4550, classified as slow rotator due to two counter-rotating discs, is shown as orange filled symbol. The one slow rotator at small $\log \sigma_e$ is NGC 4458. NGC 474, which shows star formation at larger radii and thus shows a significantly negative age gradient (see also Paper XIII and Section 4.1.1), is labelled in the age gradient panels. There is a break in the metallicity gradient versus M_{dyn} relation at a mass of $\sim 3.5 \times 10^{10} M_{\odot}$ first detected by Spolaor et al. (2009) and indicated by the thick grey line. The grey shaded area in the left-middle panel shows the approximate region occupied by the simulations of Hopkins et al. (2009a, their fig. 29).

In Fig. 16, we show the SSP equivalent age, metallicity and $[\alpha/\text{Fe}]$ versus $\log \sigma_e$, the dynamical mass M_{dyn} and $\log \lambda_R$ relations for the one R_e aperture. In agreement with Thomas et al. (2005) we find a correlation of age with velocity dispersion σ_e . This correlation is driven by the very young, low-mass galaxies ($\sigma_e < 100 \text{ km s}^{-1}$) showing widespread signs of young stellar populations and the substantial fraction of fast rotators in the intermediate-mass range which are affected to various degrees by the contribution from younger stars linked to disc-like kinematics. Since the current sample is not complete, particularly at the low-mass end, it is difficult to assess how many low-mass, old systems exist. Perhaps more importantly, the age versus dynamical mass plot shows that a strong contribution from young stellar populations is confined to the low-mass end ($\lesssim 2 \times 10^{10} M_{\odot}$). With increasing mass, the relative fraction of ‘young’ galaxies decreases because any recent star formation contributes relatively less to the total mass of the system. The slow rotators appear to be the oldest galaxies in the sample with a weak trend of decreasing λ_R and increasing SSP-equivalent age. Confirmation of this trend awaits the analysis of a larger more complete sample of slow rotators. However, there is also a substantial number of *fast* rotators for which the last star formation event was either long ago or very minor in mass fraction so that they show old SSP-equivalent ages.

In agreement with previous investigations (e.g. Kuntschner et al. 2002; Thomas et al. 2005; Bernardi et al. 2006; Collobert et al. 2006; Thomas et al. 2010) there is mild evidence for early-type galaxies residing in low-density regions to have slightly younger ages on

average compared to the cluster environment. For the SAURON sample, we find mean ages of 10.8 ± 0.8 and 9.7 ± 0.9 Gyr for cluster and field galaxies, respectively (the errors are given as errors on the mean).

In summary, massive slow rotators have typically old SSP-equivalent ages while low-mass fast rotators make up the most prominent examples of young SSP-equivalent ages. In the intermediate-mass range, galaxies show a range of SSP-equivalent ages of greater than 5 Gyr. The contributions from younger stellar populations are linked to secondary star formation in disc- or ring-like structures (see Section 4.1.1).

Despite the various, distinct components and structures we find in the stellar population maps and discuss in Section 4.1, the global, integrated metallicity estimates over one effective radius show a significant, positive correlation with $\log \sigma_e$. A linear fit, excluding NGC 3032, gives (see Fig. 16)

$$[Z/H](R_e) = 0.32(\pm 0.07) \log \sigma_e - 0.82(\pm 0.15).$$

The metallicity– $\log \sigma_e$ relation is in agreement with previous investigations (e.g. Kuntschner 2000; Thomas et al. 2005). On average we find smaller metallicities compared to the study of e.g. Thomas et al. (2005), which is caused by the larger aperture we use in our analysis (one R_e versus $R_e/10$). The most extreme case of a post starburst galaxy in our sample, NGC 3032, deviates from the relation. However, we ascribe this to the extreme luminosity weighting of young and old stars in this galaxy and therefore consider the SSP-equivalent estimate of the metallicity as not meaningful. There is

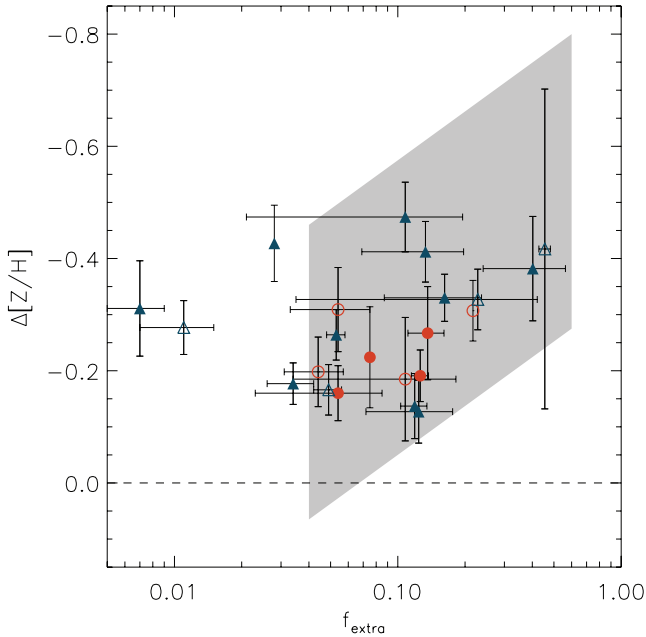


Figure 15. Metallicity gradients as derived from radial averages along isophotes *versus* f_{extra} , the fraction of extra light as determined by Hopkins et al. (2009a) for galaxies in common. The grey shaded area shows the approximate region occupied by the simulations of Hopkins et al. (2009a, their fig. 29). Fast and slow rotators are indicated by blue triangles and red circles, respectively. Cluster and field galaxies are shown as filled and open symbols. NGC 4550, classified as slow rotator due to two counter-rotating discs, is shown as the orange filled symbol.

no evidence for an environmental dependence of the metallicity– σ_e relation in our sample.

The correlation of our global (one R_e) metallicity estimates with dynamical mass M_{dyn} is significant at the 3σ level but shows a significant scatter in metallicity at a given mass (rms = 0.08 dex):

$$[Z/H] = 0.06(\pm 0.02) \log M_{\text{dyn}} - 0.75(\pm 0.25).$$

Trager et al. (2000) showed in a study of 50 local elliptical galaxies that in the four-dimensional space of metallicity, \log age, $\log \sigma$ and $[\alpha/\text{Fe}]$ only a two-dimensional plane is occupied. Furthermore, velocity dispersion seems to be the only structural parameter that determines the stellar population of a galaxy. One of the projections from this plane is the remarkably tight correlation between $[\alpha/\text{Fe}]$ and $\log \sigma$. We show our $[\alpha/\text{Fe}]$ estimates as a function of central velocity dispersion in the bottom left panel of Fig. 16. In good agreement with the literature, we find a rather tight relation in the sense that more massive galaxies exhibit larger α/Fe ratios (see also Jørgensen 1999; Kuntschner et al. 2001; Proctor & Sansom 2002; Thomas et al. 2005, 2010). We do not detect a significant difference between low- and high-density environments. The best-fitting relation for the full sample is

$$[\alpha/\text{Fe}] = 0.35(\pm 0.06) \log \sigma_e - 0.53(\pm 0.13).$$

The best-fitting relation of $[\alpha/\text{Fe}]$ with dynamical mass is

$$[\alpha/\text{Fe}] = 0.09(\pm 0.02) \log M_{\text{dyn}} - 0.70(\pm 0.20).$$

What drives the $[\alpha/\text{Fe}]$ – $\log \sigma_e$ (or mass) relation? Taking our results from Section 4.1 into account we find that the fast rotator galaxies with intermediate-velocity dispersions ($\sigma_e = 100$ – 160 km s^{-1}) are the ones with contributions of stellar populations formed in a component with disc-like kinematics and more solar $[\alpha/\text{Fe}]$ values. The

luminosity-weighted averages of the disc-like component with the main body of the galaxy results in intermediate values of $[\alpha/\text{Fe}]$. The group of galaxies with SSP-equivalent ages of < 4 Gyr have the strongest relative contribution of a young disc and SSP-equivalent estimates of $[\alpha/\text{Fe}] \simeq 0.1$ and thus determine the low-mass point of the relation. We conclude that in our sample there is evidence that the young stars with more solar-like $[\alpha/\text{Fe}]$ ratios, created in fast-rotating disc-like components in low- and intermediate-mass galaxies, reduce the global $[\alpha/\text{Fe}]$ and thus significantly contribute to the apparent $[\alpha/\text{Fe}]$ – $\log \sigma_e$ relation. However, we also find at least one low-mass galaxy (NGC 4458; $\sigma_e < 100 \text{ km s}^{-1}$), which has a $[\alpha/\text{Fe}]$ value comparable with the most massive systems in our sample.

For the slow rotators, there is evidence for a trend of increasing $[\alpha/\text{Fe}]$ with decreasing λ_R . Overall, however, the metallicity and $[\alpha/\text{Fe}]$ estimates of the slow rotators appear surprisingly inhomogeneous. Although the current sample of slow rotators is limited, the significant spread in the detailed stellar population properties may indicate that there could be more than one formation path resulting in slow rotators.

5 CONCLUDING REMARKS

We caution the reader at this point that the SAURON sample is a representative sample of limited size and not complete; therefore results for the population of early-type galaxies as a whole await confirmation with larger samples.

Nevertheless, the SSP-equivalent stellar population maps presented in this paper show that the 48 early-type galaxies in the SAURON sample display a significant and varied structure in their stellar populations. Up to 50 per cent of the sample galaxies show signs of a contribution from a young stellar population. The young stars, dominating the light, are very apparent in the low-mass ($\lesssim 3 \times 10^{10} M_\odot$) post-starburst systems, showing signs of residual star formation in the NUV and mid-IR and even optical gas emission lines consistent with star formation in the most extreme case (NGC 3032). For these systems we observe SSP-equivalent ages of ≤ 3 Gyr over the full FoV, typically covering one effective radius R_e . Spatially well localized cases of young stars in circumnuclear discs and rings are found in eight intermediate-mass systems. The latter star formation can be linked to thin, dusty discs/rings also seen by star formation signatures in the NUV or mid-IR and optical gas emission lines consistent with star formation for two galaxies (NGC 4459, NGC 4526).

About 30 per cent of the sample galaxies show intermediate SSP-equivalent ages (3–9 Gyr) where ongoing star formation is rarely detected by NUV or mid-IR signatures, suggesting that the star formation process was concluded more than ~ 1 Gyr ago. Common to most of these galaxies is the ubiquitous presence of ordered stellar motion, classifying them as fast rotators. We show that the flattened components with disc-like kinematics identified in all fast rotators (Paper XII) are connected to regions of distinct stellar populations. This is clearly seen in the examples of the very young, still star-forming circumnuclear discs and rings with increased metallicity preferentially found in intermediate-mass fast rotators (e.g. NGC 4526). However, signs of increased metallicity and mildly depressed $[\alpha/\text{Fe}]$ ratios compared with the main body of the galaxy are seen in many fast rotators extending to apparently old galaxies with extended disc-like kinematics (e.g. NGC 4660). Additionally, intermediate-mass fast rotators often show evidence for nuclear stellar discs with increased metallicity. A galaxy formation picture emerges where essentially all fast rotators have experienced,

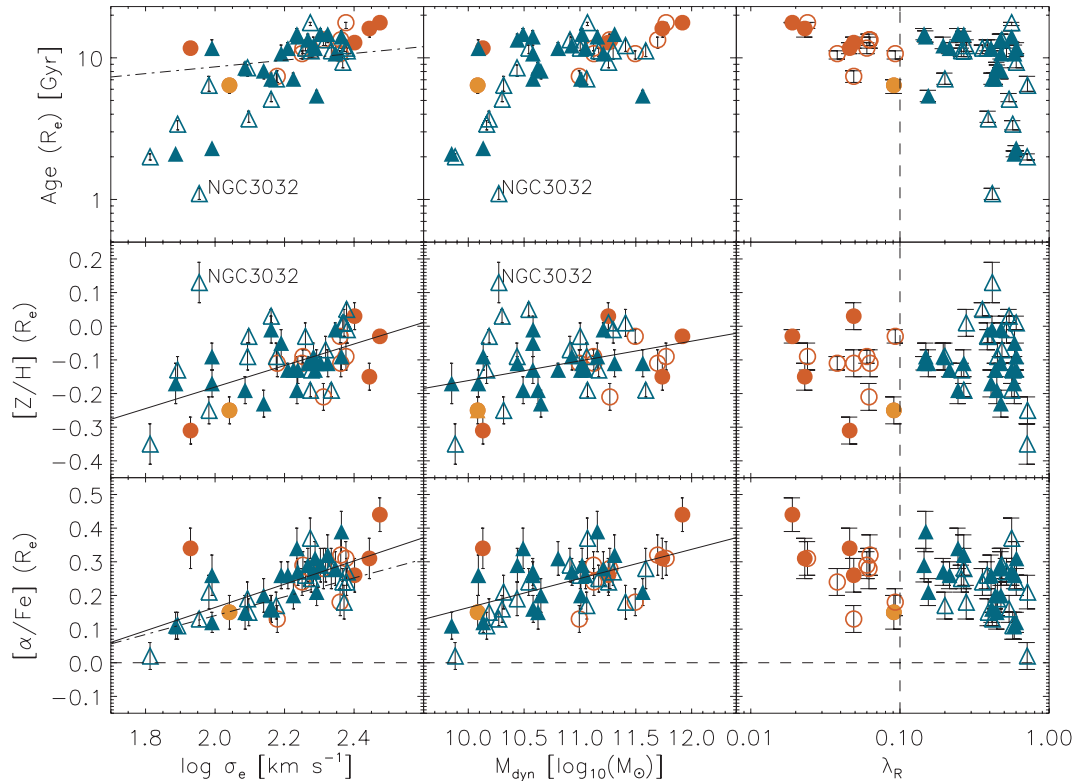


Figure 16. One effective radius, integrated measurements of SSP-equivalent age, $[Z/H]$ and $[\alpha/Fe]$ versus $\log \sigma_e$ dynamical mass M_{dyn} and $\log \lambda_R$ relations. Fast and slow rotators are indicated by blue triangles and red circles, respectively. Cluster and field galaxies are shown as filled and open symbols. NGC 4550, classified as slow rotator due to two counter-rotating discs, is shown as orange filled symbol. The dot–dashed lines in the age and $[\alpha/Fe]$ versus $\log \sigma_e$ relations are taken from Thomas et al. (2005), whereas solid lines are linear fits to our data.

often multiple, periods of secondary star formation in kinematically disc-like components on top of an older, spheroidal component.

In contrast, the slow rotators, often harbouring KDCs in their central regions, generally show no stellar population signatures over and above the well-known metallicity gradients in early-type galaxies and are largely consistent with old (≥ 10 Gyr) stellar populations.

Using our radially averaged stellar population gradients we find that low-mass fast rotators form a sequence of increasing metallicity gradient with increasing mass, consistent with the observations of Spolaor et al. (2009). For more massive systems (above $\sim 3.5 \times 10^{10} M_{\odot}$) there is an overall downturn such that metallicity gradients become shallower with increased scatter at a given mass leading to the most massive systems being slow rotators with relatively shallow metallicity gradients. The shallower metallicity gradients and increased scatter could be a consequence of the competition between different star formation and assembly scenarios following a general trend of diminishing gas fractions and more equal-mass mergers with increasing mass, leading to the most massive systems being devoid of ordered motion and any signs of recent star formation.

We also use our observations to compute more global stellar population parameters integrated over circular apertures of one-eighth and one effective radius, and compare the resulting relations of stellar population parameters versus velocity dispersion with previous results. In agreement with previous investigations, we find significant metallicity– σ and $[\alpha/Fe]$ – σ relations. The metallicity–dynamical mass relation is shallow and shows a large scatter at a given mass possibly reflecting the many different formation and assembly histories which can lead to an early-type galaxy of a

given mass. We argue that the $[\alpha/Fe]$ – σ relation is largely driven by an increasing relative contribution from metal-rich and mildly $[\alpha/Fe]$ depressed disc-like components in galaxies with decreasing mass.

ACKNOWLEDGMENTS

We would like to thank Ricardo Schiavon for providing the custom-built stellar population models with adjusted $[Ti/Fe]$ ratios and Claudia Maraston and Daniel Thomas for interesting discussions on the use of stellar population models. We are very grateful to the referee for comments that improved the quality of this manuscript. HK is grateful to Michael J. Williams for his advice on the language of the article.

The SAURON project was made possible through grants 614.13.003, 781.74.203, 614.000.301 and 614.031.015 from NWO and financial contributions from the Institut National des Sciences de l’Univers, the Université Lyon I, the Universities of Durham, Leiden and Oxford, the Programme National Galaxies, the British Council, PPARC grant ‘Observational Astrophysics at Oxford 2002–2006’ and support from Christ Church Oxford, and the Netherlands Research School for Astronomy NOVA. NS is grateful for the support of an STFC studentship. MC acknowledges support from an STFC Advanced Fellowship (PP/D005574/1). RLD is grateful for the award of a PPARC Senior Fellowship (PPA/Y/S/1999/00854), postdoctoral support through PPARC grant PPA/G/S/2000/00729 and from the Royal Society through a Wolfson Merit Award. The PPARC Visitors grant (PPA/V/S/2002/00553) to Oxford also supported this paper. GvdV acknowledges

support provided by NASA through Hubble Fellowship grant HST-HF-01202.01-A awarded by the Space Telescope Science Institute, which is operated by the Association of Universities for Research in Astronomy, Inc., for NASA, under contract NAS 5-26555. This paper is based on observations obtained at the William Herschel Telescope, operated by the Isaac Newton Group in the Spanish Observatorio del Roque de los Muchachos of the Instituto de Astrofísica de Canarias. It is also based on observations obtained at the 1.3-m McGraw-Hill Telescope at the MDM observatory on Kitt Peak, which is owned and operated by the University of Michigan, Dartmouth College, the Ohio State University, Columbia University and Ohio University. This project made use of the HyperLeda and NED data bases. Part of this work is based on *HST* data obtained from the ESO/ST-ECF Science Archive Facility.

REFERENCES

- Arimoto N., Yoshii Y., 1987, *A&A*, 173, 23
 Bacon R. et al., 2001, *MNRAS*, 326, 23 (Paper I)
 Baldry I. K., Glazebrook K., Brinkmann J., Ivezić Ž., Lupton R. H., Nichol R. C., Szalay A. S., 2004, *ApJ*, 600, 681
 Bell E. F. et al., 2004, *ApJ*, 608, 752
 Bender R., 1988, *A&A*, 202, L5
 Bernardi M., Nichol R. C., Sheth R. K., Miller C. J., Brinkmann J., 2006, *AJ*, 131, 1288
 Blanc G. A., Heiderman A., Gebhardt K., Evans N. J., Adams J., 2009, *ApJ*, 704, 842
 Bower R. G., Benson A. J., Malbon R., Helly J. C., Frenk C. S., Baugh C. M., Cole S., Lacey C. G., 2006, *MNRAS*, 370, 645
 Brough S., Proctor R., Forbes D. A., Couch W. J., Collins C. A., Burke D. J., Mann R. G., 2007, *MNRAS*, 378, 1507
 Bundy K. et al., 2006, *ApJ*, 651, 120
 Cappellari M., Copin Y., 2003, *MNRAS*, 342, 345
 Cappellari M. et al., 2006, *MNRAS*, 366, 1126 (Paper IV)
 Cappellari M. et al., 2007, *MNRAS*, 379, 418 (Paper X)
 Carlberg R. G., 1984, *ApJ*, 286, 403
 Carollo C. M., Danziger I. J., Buson L., 1993, *MNRAS*, 265, 553
 Chilingarian I. V., 2009, *MNRAS*, 394, 1229
 Cimatti A., Daddi E., Renzini A., 2006, *A&A*, 453, L29
 Cole S., Lacey C. G., Baugh C. M., Frenk C. S., 2000, *MNRAS*, 319, 168
 Collobert M., Sarzi M., Davies R. L., Kuntschner H., Colless M., 2006, *MNRAS*, 370, 1213
 Combes F., Young L. M., Bureau M., 2007, *MNRAS*, 377, 1795
 Crocker A. F., Bureau M., Young L. M., Combes F., 2008, *MNRAS*, 386, 1811
 Crocker A. F., Jeong H., Komugi S., Combes F., Bureau M., Young L. M., Yi S., 2009, *MNRAS*, 393, 1255
 Davies R. L., Sadler E. M., Peletier R. F., 1993, *MNRAS*, 262, 650
 Davies R. L. et al., 2001, *ApJ*, 548, L33
 De Lucia G., Springel V., White S. D. M., Croton D., Kauffmann G., 2006, *MNRAS*, 366, 499
 de Zeeuw P. T. et al., 2002, *MNRAS*, 329, 513 (Paper II)
 Elmegreen B. G., Bournaud F., Elmegreen D. M., 2008, *ApJ*, 688, 67
 Emsellem E. et al., 2004, *MNRAS*, 352, 721 (Paper III)
 Emsellem E. et al., 2007, *MNRAS*, 379, 401 (Paper IX)
 Faber S. M. et al., 2007, *ApJ*, 665, 265
 Fisher D., Franx M., Illingworth G., 1996, *ApJ*, 459, 110
 Fitzpatrick E. L., 1999, *PASP*, 111, 63
 Genzel R. et al., 2008, *ApJ*, 687, 59
 González J. J., 1993, PhD thesis, Univ. California
 Graves G. J., Schiavon R. P., 2008, *ApJS*, 177, 446
 Hoffman L., Cox T. J., Dutta S., Hernquist L., 2009, *ApJ*, 705, 920
 Hopkins P. F., Cox T. J., Dutta S. N., Hernquist L., Kormendy J., Lauer T. R., 2009a, *ApJS*, 181, 135
 Hopkins P. F., Lauer T. R., Cox T. J., Hernquist L., Kormendy J., 2009b, *ApJS*, 181, 486
 Jeong H., Bureau M., Yi S. K., Krajnović D., Davies R. L., 2007, *MNRAS*, 376, 1021
 Jeong H. et al., 2009, *MNRAS*, 398, 2028 (Paper XIII)
 Jones L. A., 1999, PhD thesis, Univ. North Carolina
 Jørgensen I., 1999, *MNRAS*, 306, 607
 Kaviraj S., Peirani S., Khochfar S., Silk J., Kay S., 2009, *MNRAS*, 394, 1713
 Kobayashi C., 2004, *MNRAS*, 347, 740
 Korn A. J., Maraston C., Thomas D., 2005, *A&A*, 438, 685
 Krajnović D., Cappellari M., de Zeeuw P. T., Copin Y., 2006, *MNRAS*, 366, 787
 Krajnović D. et al., 2008, *MNRAS*, 390, 93 (Paper XII)
 Kuntschner H., 2000, *MNRAS*, 315, 184
 Kuntschner H., Lucey J. R., Smith R. J., Hudson M. J., Davies R. L., 2001, *MNRAS*, 323, 615
 Kuntschner H., Smith R. J., Colless M., Davies R. L., Kaldare R., Vazdekis A., 2002, *MNRAS*, 337, 172
 Kuntschner H. et al., 2006, *MNRAS*, 369, 497 (Paper VI)
 Lauer T. R. et al., 2005, *AJ*, 129, 2138
 Lee H.-c., Worthey G., 2005, *ApJS*, 160, 176
 Marchesini D., van Dokkum P. G., Förster Schreiber N. M., Franx M., Labbé I., Wuyts S., 2009, *ApJ*, 701, 1765
 McDermid R. M. et al., 2006, *MNRAS*, 373, 906 (Paper VIII)
 Norris M. A., Sharples R. M., Kuntschner H., 2006, *MNRAS*, 367, 815
 O’Connell R. W., 1999, *ARA&A*, 37, 603
 Pipino A., D’Ercole A., Matteucci F., 2008, *A&A*, 484, 679
 Pracy M. B., Kuntschner H., Couch W. J., Blake C., Bekki K., Briggs F., 2009, *MNRAS*, 396, 1349
 Press W. H., Teukolsky S. A., Vetterling W. T., Flannery B. P., 1992, *Numerical Recipes in FORTRAN. The Art of Scientific Computing*. University Press, Cambridge
 Proctor R. N., Sansom A. E., 2002, *MNRAS*, 333, 517
 Proctor R. N., Forbes D. A., Beasley M. A., 2004, *MNRAS*, 355, 1327
 Rawle T. D., Smith R. J., Lucey J. R., Swinbank A. M., 2008, *MNRAS*, 389, 1891
 Rawle T. D., Smith R. J., Lucey J. R., 2010, *MNRAS*, 401, 852
 Sansom A. E., Northeast M. S., 2008, *MNRAS*, 387, 331
 Sánchez-Blázquez P. et al., 2006, *MNRAS*, 371, 703
 Sánchez-Blázquez P., Forbes D. A., Strader J., Brodie J., Proctor R., 2007, *MNRAS*, 377, 759
 Sarzi M. et al., 2006, *MNRAS*, 366, 1151 (Paper V)
 Sarzi M. et al., 2010, *MNRAS*, 402, 2187 (Paper XVI)
 Schawinski K., Thomas D., Sarzi M., Maraston C., Kaviraj S., Joo S.-J., Yi S. K., Silk J., 2007, *MNRAS*, 382, 1415
 Schiavon R. P., 2007, *ApJS*, 171, 146
 Scott N. et al., 2009, *MNRAS*, 398, 1835 (Paper XIV)
 Serra P., Trager S. C., 2007, *MNRAS*, 374, 769
 Shapiro K. L. et al., 2010, *MNRAS*, 402, 2140 (Paper XV)
 Smith R. J., Lucey J. R., Hudson M. J., Allanson S. P., Bridges T. J., Hornschemeier A. E., Marzke R. O., Miller N. A., 2009, *MNRAS*, 392, 1265
 Somerville R. S., Primack J. R., 1999, *MNRAS*, 310, 1087
 Spolaor M., Proctor R. N., Forbes D. A., Couch W. J., 2009, *ApJ*, 691, L138
 Thomas D., Maraston C., Bender R., 2003, *MNRAS*, 339, 897 (TMB03)
 Thomas D., Maraston C., Bender R., de Oliveira C. M., 2005, *ApJ*, 621, 673
 Thomas D., Maraston C., Schawinski K., Sarzi M., Silk J., 2010, *MNRAS*, 404, 1775
 Trager S. C., Faber S. M., Worthey G., González J. J., 2000, *AJ*, 120, 165
 Trager S. C., Faber S. M., Dressler A., 2008, *MNRAS*, 386, 715
 Treu T. et al., 2005, *ApJ*, 633, 174
 Turnbull A. J., Bridges T. J., Carter D., 1999, *MNRAS*, 307, 967
 van den Bosch F. C., Emsellem E., 1998, *MNRAS*, 298, 267
 van den Bosch R. C. E., van de Ven G., Verolme E. K., Cappellari M., de Zeeuw P. T., 2008, *MNRAS*, 385, 647
 van der Wel A., Rix H., Holden B. P., Bell E. F., Robaina A. R., 2009, *ApJ*, 706, L120

- Vazdekis A., Peletier R. F., Beckman J. E., Casuso E., 1997, ApJS, 111, 203
 Vazdekis A., Sánchez-Blázquez P., Falcón-Barroso J., Cenarro A. J., Beasley M. A., Cardiel N., Gorgas J., Peletier R. F., 2010, MNRAS, 404, 1639
 Weijmans A., Krajnović D., van de Ven G., Oosterloo T. A., Morganti R., de Zeeuw P. T., 2008, MNRAS, 383, 1343
 White S. D. M., 1980, MNRAS, 191, 1P
 Willmer C. N. A. et al., 2006, ApJ, 647, 853
 Worthey G., 1994, ApJS, 95, 107
 Worthey G., Faber S. M., Gonzalez J. J., Burstein D., 1994, ApJS, 94, 687
 Yamada Y., Arimoto N., Vazdekis A., Peletier R. F., 2006, ApJ, 637, 200
 York D. G. et al., 2000, AJ, 120, 1579
 Young L. M., Bureau M., Cappellari M., 2008, ApJ, 676, 317

APPENDIX A: REVISED LINE STRENGTH MEASUREMENTS FOR CIRCULAR APERTURES OF $R_e/8$ AND R_e

We present revised line strength measurements on the Lick/IDS system over circular apertures of $R_e/8$ and R_e in Table A1. This table supersedes the data presented in table 5 of Paper VI. The details of the revised data reduction are given in Section 2. We further note that the effective radius values were revised using an $R^{1/n}$ growth curve analysis of our wide-field MDM (1.3 m) imaging survey of the early-type galaxy sample (Falcón-Barroso, in preparation).

Table A1. List of revised line strength measurements within a circular aperture of $R_e/8$ and R_e .

Name	R_e (arcsec)	σ (km s^{-1})	H β (\AA)	Fe5015 (\AA)	Mg <i>b</i> (\AA)	Fe5270 _S (\AA)	σ_e (km s^{-1})	H β (\AA)	Fe5015 (\AA)	Mg <i>b</i> (\AA)
Aperture (1)	(2)	$R_e/8$ (3)	$R_e/8$ (4)	$R_e/8$ (5)	$R_e/8$ (6)	$R_e/8$ (7)	R_e (8)	R_e (9)	R_e (10)	R_e (11)
NGC 474	28.0	166	1.66	5.33	4.08	–	142	1.82	4.79	3.44
NGC 524	35.4	251	1.34	5.43	4.50	–	225	1.48	5.35	4.22
NGC 821	31.3	200	1.52	5.31	4.38	–	182	1.59	4.67	3.75
NGC 1023	48.7	204	1.49	5.46	4.45	2.33	165	1.51	4.96	4.12
NGC 2549	13.9	148	2.04	5.93	4.12	2.44	140	1.96	5.15	3.59
NGC 2685	23.6	90	1.99	4.94	3.52	2.17	100	1.91	4.20	3.00
NGC 2695	18.7	222	1.31	5.03	4.58	–	184	1.26	4.33	3.95
NGC 2699	12.1	150	1.79	5.79	4.29	2.42	123	1.75	4.81	3.60
NGC 2768	68.0	205	1.68	4.96	4.06	–	200	1.60	4.43	3.62
NGC 2974	28.3	237	1.64	5.16	4.42	2.27	227	1.66	5.02	4.05
NGC 3032	19.3	94	4.77	4.47	1.71	1.61	90	3.86	4.08	2.20
NGC 3156	14.8	66	4.44	3.88	1.54	1.58	66	2.98	3.78	1.84
NGC 3377	38.3	144	1.83	4.88	3.81	2.08	126	1.80	4.37	3.18
NGC 3379	44.9	216	1.39	5.12	4.51	2.19	190	1.43	4.74	4.10
NGC 3384	28.5	161	1.85	5.81	4.14	2.46	141	1.82	5.07	3.68
NGC 3414	32.0	232	1.42	4.99	4.51	2.17	191	1.49	4.46	3.70
NGC 3489	21.5	105	2.81	4.93	2.82	2.01	99	2.60	4.37	2.58
NGC 3608	33.6	191	1.51	5.25	4.39	–	167	1.61	4.74	3.77
NGC 4150	15.9	83	3.53	4.22	2.16	1.69	77	2.82	4.13	2.35
NGC 4262	10.6	196	1.41	4.94	4.45	2.06	164	1.45	4.41	3.85
NGC 4270	13.7	138	1.75	5.15	3.49	–	125	1.75	4.60	3.26
NGC 4278	30.6	252	1.28	4.69	4.70	2.11	217	1.44	4.51	4.17
NGC 4374	70.2	292	1.38	5.08	4.52	2.24	261	1.40	4.61	4.07
NGC 4382	94.4	187	2.11	5.06	3.45	2.11	178	1.99	4.60	3.27
NGC 4387	11.0	100	1.62	5.07	3.95	2.22	98	1.54	4.54	3.69
NGC 4458	19.9	106	1.61	4.60	3.82	1.92	83	1.61	4.05	3.33
NGC 4459	41.0	178	2.14	5.25	3.85	2.26	155	1.84	4.60	3.37
NGC 4473	26.8	192	1.49	5.37	4.51	2.31	186	1.50	4.78	3.98
NGC 4477	46.5	170	1.62	5.06	4.14	2.22	147	1.55	4.67	3.81
NGC 4486	106.2	311	1.15	5.15	5.11	2.25	268	1.15	4.59	4.59
NGC 4526	35.7	232	1.84	5.51	4.31	2.32	214	1.58	4.91	4.16
NGC 4546	22.0	220	1.54	5.34	4.60	2.28	189	1.54	4.56	3.87
NGC 4550	11.6	88	2.11	4.54	3.17	2.00	103	1.92	4.35	2.96
NGC 4552	33.9	268	1.55	5.65	4.83	2.29	233	1.45	5.14	4.40
NGC 4564	19.3	173	1.52	5.87	4.77	2.42	150	1.57	4.84	4.00
NGC 4570	12.8	197	1.45	5.80	4.67	2.33	167	1.45	4.75	3.97
NGC 4621	46.0	225	1.40	5.29	4.68	2.27	200	1.44	4.67	4.11
NGC 4660	11.5	221	1.43	5.56	4.76	2.30	181	1.47	4.71	4.02
NGC 5198	18.0	206	1.46	5.44	4.73	–	173	1.55	4.72	3.97
NGC 5308	9.9	244	1.46	5.28	4.46	–	201	1.46	4.83	4.16
NGC 5813	55.9	226	1.49	5.00	4.47	2.12	210	1.49	4.63	4.03
NGC 5831	29.2	168	1.72	5.55	4.13	2.38	148	1.81	4.83	3.34
NGC 5838	20.6	283	1.59	5.68	4.60	2.38	232	1.57	4.96	4.17
NGC 5845	4.3	269	1.51	5.62	4.64	2.30	237	1.51	5.23	4.36

Table A1 – *continued*

Name	R_e (arcsec)	σ (km s ⁻¹)	H β (Å)	Fe5015 (Å)	Mg <i>b</i> (Å)	Fe5270 _S (Å)	σ_e (km s ⁻¹)	H β (Å)	Fe5015 (Å)	Mg <i>b</i> (Å)
Aperture (1)	(2)	$R_e/8$ (3)	$R_e/8$ (4)	$R_e/8$ (5)	$R_e/8$ (6)	$R_e/8$ (7)	R_e (8)	R_e (9)	R_e (10)	R_e (11)
NGC 5846	76.8	236	1.33	5.37	4.80	–	213	1.30	4.83	4.34
NGC 5982	24.9	260	1.62	5.74	4.41	–	223	1.59	5.11	3.95
NGC 7332	9.2	137	2.27	5.87	3.67	2.28	125	2.14	4.85	3.19
NGC 7457	33.2	70	2.37	4.98	2.92	2.09	75	2.25	4.56	2.80

Notes: This table supersedes the values published in table 5 of Paper VI. (1) NGC number. (2) Effective (half-light) radius R_e measured with a $R^{1/n}$ growth curve analysis from our wide-field MDM (1.3 m) imaging survey of the early-type galaxy sample (Falcón-Barroso, in preparation). (3) Velocity dispersion of the luminosity-weighted spectrum within a circular aperture of $R_e/8$. Only the first two moments, v and σ , are used in the fit to the spectrum. (4)–(7) Fully corrected line strength index measurements on the Lick/IDS system of the luminosity-weighted spectrum within $R_e/8$ for the H β , Fe5015, Mg *b* and Fe5270_S indices. Due to a limited field coverage we cannot determine the Fe5270_S indices for 11 galaxies. (8) Velocity dispersion of the luminosity-weighted spectrum within a circular aperture of one R_e . Only the first two moments, v and σ , are used in the fit to the spectrum. (9)–(11) Fully corrected line strength index measurements on the Lick/IDS system of the luminosity-weighted spectrum within R_e for the H β , Fe5015 and Mg *b* indices. For galaxies with less than one R_e coverage, we applied the aperture corrections given in Paper VI. Formal errors of the line strength indices are below 0.1 Å. We note, however, that there are systematic errors which we estimate to be of the order of 0.06, 0.15, 0.08, 0.06 Å for the H β , Fe5015, Mg *b* and Fe5270_S indices, respectively. For the velocity dispersion we adopt an error of 5 per cent.

This paper has been typeset from a \LaTeX file prepared by the author.